ARTICLES

Dynamical Chirality and the Quantum Dynamics of Bending Vibrations of the CH Chromophore in Methane Isotopomers‡

Roberto Marquardt,† Martin Quack,* and Ioannis Thanopulos

Laboratorium für Physikalische Chemie, ETH-Zürich (Zentrum), 8092 - Zürich, Switzerland

Received: December 2, 1999; In Final Form: March 7, 2000

The time-dependent quantum dynamics of the CH chromophore is investigated by calculations of the wave packet evolution after coherent excitation of the bending modes using realistic potential energy surfaces and electric dipole moment functions for the methane isotopomers CHD_3, CHD_2T, and $CHDT_2$ derived previously from ab initio calculations and high-resolution spectroscopic information. Results include discussions on different excitation pathways depending on the bending direction in an internal coordinate frame, the role of quasiclassical and delocalized intramolecular vibrational redistribution on these processes, and a possibility of controlling the dynamics by localization of the wave packet motion in subspaces of the relevant configuration space. Bending excitation is also used to generate dynamical chirality, which is quantified by the enantiomeric excess. The subsequent free evolution of the wave packet after generation of a chiral molecular structure corresponds to a stereomutation reaction on the femtosecond time scale superimposed by a racemization reaction, which is understood as arising from quantum delocalization effects due to intramolecular vibrational redistribution.

1. Introduction

The study of the primary physical processes of intramolecular dynamics on the femtosecond time scale is a fundamental step toward the understanding of molecular structure, its time dependence, and, potentially, the subsequent chemical reaction dynamics.[1] The investigation of such processes has become an important modern branch of chemical kinetics, as demonstrated by the attention received in a series of conferences and special issues during the last two decades.[2−9] One approach to this investigation aims at the observation of structural changes during the chemical reaction with time-resolved spectroscopic techniques[10−15] ("time-dependent approach") with much current emphasis on condensed-phase work and biochemical processes.[16−22] In a second, "time-independent" approach,[23] the nuclear motion is determined from the analysis of experimental data from time-independent high-resolution spectroscopy by calculation of the molecular quantum dynamics. It is in the context of this approach that, during nearly two decades, work in our and in other laboratories has been directed toward the study of the short-time primary intramolecular dynamics of CH chromophores in polyatomic organic molecules (see for instance the reviews[24−29]). The present investigation is carried out with a similar goal in mind but stresses quite new aspects of dynamical chirality.

The intramolecular vibrational redistribution (IVR) between the stretching and bending vibrations of the alkyl CH chromophore is one of the essential primary processes (see refs 24−27 and 30 for recent reviews on some basic concepts and also some critical discussion of current misconceptions of IVR). Of particular importance is the determination of the wave packet motion in configuration space to obtain the full information on the time evolution of state populations and relative phases in the underlying quantum dynamics.[30,31] In this context, one early result for the manifestation of IVR was that the initial excitation of a narrow range of energies, ideally localized along one of the possible vibrational manifolds of the alkyl CH chromophore in CHF_3 and CHD_3, would lead to a spreading of the probability density distribution in configuration space toward a quasimicrocanonical distribution in less than 1 ps.[31] In further investigations,[32−34] the coherent infrared multiphoton excitation of states in the stretching manfold was investigated, which led to an initially semiclassical motion of the wave packet, localized along the stretching coordinate, and occupation of the bending manifolds after 100−500 fs by an irregular spreading of the probability density.

In the present work we ask: What is the motion of the wave packet of the alkyl CH chromophore if the excitation occurs along the bending manifolds? The answer to this question has potential immediate consequences for two current aspects of our interest in molecular dynamics: (i) the generation of dynamical chirality and the nature of vibrationally induced stereomutation and racemization dynamics;[35] (ii) the (coherent) control of the wave packet dynamics and mode-selective laser chemistry[36−43] (see also ref 44 and many other contributions in ref 7).

In each of these aspects, the intramolecular vibrational redistribution can play an important role, and the investigation

* Corresponding author. Fax: 0041-1-6321021. E-mail: Quack@ir.phys.chem.ethz.ch.

† Permanent address: Universite de Marne-la-Vallee, 5 Bd Descartes, 77454 Champs-sur-Marne, France.

‡ This article was originally submitted for publication in the Time Resolved Vibrational Spectroscopy Special issue.

10.1021/jp994245d CCC: $19.00
Published on Web 06/10/2000

of the vibrational dynamics in the CH chromophore subspace provides a realistic platform for this discussion.

In this context, we will also discuss the nature of the nearly isoenergetic effective Hamiltonian wave functions (basis states) of the alkyl CH chromophore, which are strongly coupled by a 2:1 Fermi resonance. Effective basis states are frequently used to study the quantum dynamics with effective Hamiltonians to describe the data derived from high-resolution spectroscopy, and a recent example of this is the investigation of large amplitude bending motion of acetylene,[45] quite related to our own work.[24] However, the relation of such basis states to true molecular wave functions, which can be defined as projections on configuration space, is often difficult to establish when the underlying potential energy surface is unknown. In the case of the effective basis states for the alkyl CH chromophore, these wave functions have been studied in previous publications,[32,46] where they were called "Fermi modes". However, some questions remained open and are addressed in the present work.

Dynamical chirality can be defined by a time-dependent non planar molecular structure of C_1 symmetry[35] (some other symmetries, such as C_2 are chiral as well). In principle, any molecular structure with C_1 symmetry is chiral, where two chiral enantiomers are defined by their relation through inversion of the coordinates of all atoms at the origin. The observable "chirality" quantum number can be introduced,[39,47] which takes the values L for left-handed and R for right-handed. The probabilities P_L and $P_R = 1 - P_L$ are time-dependent functions, which can be used to define the time-dependent absolute degree of chirality (or enantiomeric excess)

$$D_{abs} = |P_L - P_R| \tag{1}$$

The type of time evolution of this quantity can, in principle, range between periodic stereomutation and racemization. Perhaps the most obvious approach to study dynamical chirality would consider molecules that are chiral in their equilibrium geometries, but show fast tunneling stereomutation because of a low barrier for enantiomerization. Recent examples for this are the spectroscopic and exact dimensional quantum wave packet study in H_2O_2 isotopomers[40,41] as well as stereomutation in aniline-NHD.[42,43] Less obvious examples, studied here, are molecules that are achiral in their equilibrium geometries. Questions are then: How fast are stereomutation and racemization processes? If racemization exists, how is it related to the intramolecular dynamics? These questions could be addressed by studying the dynamical chirality induced for instance by localized stretching excitations of CH bonds in CH_2FD ("local modes",[48] see ref 35). In the present work, dynamical chirality is generated by preparation of dissymmetric (C_1) molecular structures through excitation of the bending modes perpendicular to the C_s mirror planes in $CHXY_2$ type of molecules. The two enantiomers can then be interconverted one into the other by mirroring at the symmetry plane.

Coherent infrared multiphoton excitation of polyatomic molecules is one possibility of controlling nuclear motion,[49,50] and has been explored in the past, to some extent, by calculation of the wave packet motion of forced one-dimensional harmonic and anharmonic oscillators.[51,52] In our previous work on the coherent multiphoton excitation of the CH chromophore,[32] we have concluded that the wave packet can be forced to move semiclassically along the stretching manifold at least during the initial 50−100 fs of the excitation process. The semiclassical motion is destroyed thereafter due to the strong anharmonic couplings. In ref 25, this was called "delocalization by intramolecular vibrational redistribution" (DIVR), in contrast to the quasiclassical intramolecular vibrational redistribution (CIVR), inferred a long time ago.[53] For a model system of very weakly coupled stretching and bending vibrations, CIVR was observed.[32] In the present work we shall explore the possibility of forcing the wave packet to move along the bending manifold and discuss the relationship of DIVR and CIVR with regard to the control of nuclear motion and time-dependent molecular structure.

Our method for determining the nuclear motion has been described in-depth several times.[24,25,54] Specifically for the present investigation, we will study the vibrational short time dynamics of the CH chromophore in isotopically substituted methanes CHD_3, CHD_2T, and $CHDT_2$. To study the bending excitation, we have used realistic potential energy[55] and dipole moment surfaces[56] of methane, which are available as global, analytical, nine-dimensional hypersurfaces able to describe nuclear motion of large amplitudes. The multiphoton excitation process and wave packet dynamics of the CH chromophore were calculated within the program package URIMIR,[57,58] using spectroscopic states obtained by calculation of the CH chromophore eigenstates on the potential energy surface within a three-dimensional DVR calculation[59,60] and transition moments as corresponding matrix elements of the dipole moment surface. Details of the method of calculation are described in Section 2.

2. Theory

2.1. Potential Energy and Dipole Moment Surface. The three-dimensional subspace of the CH chromophore in CHD_3, CHD_2T, and $CHDT_2$ is spanned by the mass-weighted normal coordinates Q_s, Q_{b_1}, and Q_{b_2}. These were obtained from a complete normal coordinate analysis of the global potential surface. The results from this analysis are listed in Table 1, including the cartesian displacement matrix $\boldsymbol{l}$ together with masses, the equilibrium geometry, and wave numbers of normal vibrations, which correspond to the currently best available, experimentally determined values.[56,61]

In CHD_2T $Q_s = Q_1$, $Q_{b_1} = Q_6$, $Q_{b_2} = Q_5$, in $CHDT_2$ $Q_s = Q_1$, $Q_{b_1} = Q_5$, $Q_{b_2} = Q_6$, and in CHD_3 $Q_s = Q_1$, $Q_{b_1} = Q_6$, $Q_{b_2} = Q_5$, such that $Q_{b_1} \sim x$ corresponds to an in-plane bending motion and $Q_{b_2} \sim y$ to an out-of-plane bending motion relative to a C_s mirror plane (see Figure 1 and Table 1).

The potential energy used has been defined as METPOT 3 in ref 55 as a function of the bond angles and bond lengths in methane. In order to obtain the reduced potential $V(Q_s, Q_{b_1}, Q_{b_2})$, we first calculated the cartesian coordinates

$$x_{n_k} = x_{n_k}^{eq} + \sum_{j=1}^{9} l_{n_k j} Q_j \tag{2}$$

(for $n = 1, ..., 5$, the number of atoms, and $k = 1, ..., 3$, the three directions of space) in the space of normal coordinates for the CH chromophore. Then we calculated the bond lengths

$$r_n = \sqrt{\sum_k (x_{n_k} - x_{5_k})^2} \tag{3}$$

for $n = 1, ..., 4$ ($n = 5$ being the central carbon atom) and bond angles

$$\alpha_{ij} = \arccos\left(\frac{\sum_k (x_{i_k} - x_{5_k})(x_{j_k} - x_{5_k})}{r_i r_j}\right) \tag{4}$$

TABLE 1: Harmonic Wavenumbers[a] (in cm^{-1}) and *l* Matrix (l_{ij}, in u$^{-1/2}$)

	j								
i[b]	1 (3128.)	2 (2336.)	3 (2336.)	4 (2185.)	5 (1335.)	6 (1335.)	7 (1070.)	8 (1070.)	9 (1042.)
					CHD_3				
d*x*(*H*) 1	0.000000	0.000000	0.010119	0.000000	0.000000	0.812715	0.148452	0.000000	0.000000
d*y*(*H*) 2	0.000000	0.010119	0.000000	0.000000	−0.812715	0.000000	0.000000	−0.148452	0.000000
d*z*(*H*) 3	0.956000	0.000000	0.000000	−0.105105	0.000000	0.000000	0.000000	0.000000	0.121485
d*x*(*D*) 4	0.020902	0.000000	−0.491165	0.373889	0.000000	0.049341	−0.128815	0.000000	0.158992
d*y*(*D*) 5	0.000000	0.004311	0.000000	0.000000	0.072595	0.000000	0.000000	−0.504958	0.000000
d*z*(*D*) 6	−0.001131	0.000000	−0.175709	0.131607	0.000000	−0.295795	0.080458	0.000000	−0.309342
d*x*(*D*) 7	−0.010451	−0.214547	−0.119558	−0.186944	−0.052800	−0.042111	0.346514	0.274432	−0.079496
d*y*(*D*) 8	−0.018102	−0.367296	−0.214547	−0.323797	−0.018857	0.052800	−0.274432	−0.029628	−0.137691
d*z*(*D*) 9	−0.001131	0.152169	0.087855	0.131607	−0.256166	0.147898	−0.040229	0.069678	−0.309342
d*x*(*D*) 10	−0.010451	0.214547	−0.119558	−0.186944	0.052800	−0.042111	0.346514	−0.274432	−0.079496
d*y*(*D*) 11	0.018102	−0.367296	0.214547	0.323797	−0.018857	−0.052800	0.274432	−0.029628	0.137691
d*z*(*D*) 12	−0.001131	−0.152169	0.087855	0.131607	0.256166	0.147898	−0.040229	−0.069678	−0.309342
d*x*(*C*) 13	0.000000	0.000000	0.121716	0.000000	0.000000	−0.062402	−0.107162	0.000000	0.000000
d*y*(*C*) 14	0.000000	0.121716	0.000000	0.000000	0.062402	0.000000	0.000000	0.107162	0.000000
d*z*(*C*) 15	−0.079721	0.000000	0.000000	−0.057437	0.000000	0.000000	0.000000	0.000000	0.145551

		equilibrium geometry (Å)		
	masses(u)	$x_{n_1}^{eq} \equiv x_n^{eq}$	$x_{n_2}^{eq} \equiv y_n^{eq}$	$x_{n_3}^{eq} \equiv z_n^{eq}$
H	1.007825	0.000000	0.000000	1.085800
D	2.014000	-1.023702	0.000000	−0.361933
D	2.014000	0.511851	0.886552	−0.361933
D	2.014000	0.511851	−0.886552	−0.361933
C	12.000000	0.000000	0.000000	0.000000

	j								
i[b]	1 (3127.63)	2 (2336.26)	3 (2254.17)	4 (1913.67)	5 (1335.46)	6 (1298.42)	7 (1064.15)	8 (987.54)	9 (973.56)
					CHD_2T				
d*x*(*H*) 1	−0.000094	0.000000	−0.004977	0.015352	0.000000	0.832574	0.141577	−0.106611	0.000000
d*y*(*H*) 2	0.000000	0.010143	0.000000	0.000000	−0.818115	0.000000	0.000000	0.000000	−0.115927
d*z*(*H*) 3	0.956413	0.000000	0.070771	−0.076631	0.000000	−0.007957	0.033373	−0.123113	0.000000
d*x*(*T*) 4	0.010891	0.000000	0.096899	0.475303	0.000000	−0.008529	−0.086024	−0.158814	0.000000
d*y*(*T*) 5	0.000000	0.002750	0.000000	0.000000	0.037071	0.000000	0.000000	0.000000	−0.373025
d*z*(*T*) 6	−0.001712	0.000000	0.035441	0.167787	0.000000	−0.188347	−0.009659	0.251762	0.000000
d*x*(*D*) 7	−0.010425	−0.214442	0.213378	−0.057827	−0.043574	−0.022711	0.318047	0.184840	0.304784
d*y*(*D*) 8	−0.018313	−0.367307	0.373348	−0.110067	−0.019957	0.062255	−0.299060	0.055773	−0.030721
d*z*(*D*) 9	−0.001009	0.152220	−0.151752	0.048651	−0.253886	0.180417	−0.118667	0.273823	0.091045
dx(D) 10	−0.010425	0.214442	0.213378	−0.057827	0.043574	−0.022711	0.318047	0.184840	−0.304784
d*y*(*D*) 11	0.018313	−0.367307	−0.373348	0.110067	−0.019957	−0.062255	0.299060	−0.055773	−0.030721
d*z*(*D*) 12	−0.001009	−0.152220	−0.151752	0.048651	0.253886	0.180417	−0.118667	0.273823	−0.091045
d*x*(*C*) 13	0.000770	0.000000	−0.095560	−0.101340	0.000000	−0.060157	−0.097027	−0.013175	0.000000
d*y*(*C*) 14	0.000000	0.121750	0.000000	0.000000	0.066091	0.000000	0.000000	0.000000	0.113803
d*z*(*C*) 15	−0.079556	0.000000	0.036087	−0.052066	0.000000	−0.012553	0.039457	−0.144851	0.000000

		equilibrium geometry (Å)		
	masses(u)	$x_{n_1}^{eq} \equiv x_n^{eq}$	$x_{n_2}^{eq} \equiv y_n^{eq}$	$x_{n_3}^{eq} \equiv z_n^{eq}$
H	1.007825	0.000000	0.000000	1.085800
T	3.016050	−1.023702	0.000000	−0.361933
D	2.014000	0.511851	0.886552	−0.361933
D	2.014000	0.511851	−0.886552	−0.361933
C	12.000000	0.000000	0.000000	0.000000

	j								
i[b]	1 (3127.27)	2 (2299.91)	3 (1994.00)	4 (1856.43)	5 (1316.27)	6 (1273.12)	7 (1004.87)	8 (959.31)	9 (902.62)
					$CHDT_2$				
d*x*(*H*) 1	0.000090	−0.007859	0.000000	0.014812	−0.825874	0.000000	0.000000	−0.147692	−0.025329
d*y*(*H*) 2	0.000000	0.000000	−0.012138	0.000000	0.000000	−0.860274	0.057026	0.000000	0.000000
d*z*(*H*) 3	0.956843	−0.046296	0.000000	0.092639	−0.005247	0.000000	0.000000	0.119650	−0.060888
d*x*(*D*) 4	0.021245	0.602069	0.000000	−0.137653	−0.059515	0.000000	0.000000	0.216526	0.058745
d*y*(*D*) 5	0.000000	0.000000	−0.004779	0.000000	0.000000	0.036376	0.544255	0.000000	0.000000
d*z*(*D*) 6	−0.000883	0.213914	0.000000	−0.057209	0.317807	0.000000	0.000000	−0.312252	0.025384
d*x*(*T*) 7	−0.005559	0.023918	−0.164244	0.177850	0.028793	−0.011686	−0.211583	−0.169101	−0.208233
d*y*(*T*) 8	−0.009462	0.045070	−0.287669	0.302952	−0.002296	0.004050	−0.003040	−0.005149	0.268043
d*z*(*T*) 9	−0.001643	−0.018996	0.115608	−0.126213	−0.086799	−0.182647	−0.061275	−0.192403	0.141348
d*x*(*T*) 10	−0.005559	0.023918	0.164244	0.177850	0.028793	0.011686	0.211583	−0.169101	−0.208233
d*y*(*T*) 11	0.009462	−0.045070	−0.287669	−0.302952	0.002296	0.004050	−0.003040	0.005149	−0.268043
d*z*(*T*) 12	−0.001643	−0.018996	−0.115608	−0.126213	−0.086799	0.182647	0.061275	−0.192403	0.141348
d*x*(*C*) 13	−0.000779	−0.112410	0.000000	−0.067542	0.064876	0.000000	0.000000	0.061067	0.096942
d*x*(*C*) 14	0.000000	0.000000	0.146426	0.000000	0.000000	0.064109	−0.094605	0.000000	0.000000
d*z*(*C*) 15	−0.079387	−0.022465	0.000000	0.065266	−0.009266	0.000000	0.000000	0.139074	−0.070199

TABLE 1: (Continued)

	masses(u)	equilibrium geometry (Å)		
		$x_{n_1}^{eq} \equiv x_n^{eq}$	$x_{n_2}^{eq} \equiv y_n^{eq}$	$x_{n_3}^{eq} \equiv z_n^{eq}$
H	1.007825	0.000000	0.000000	1.085800
D	2.014000	−1.023702	0.000000	−0.361933
T	3.016050	0.511851	0.886552	−0.361933
T	3.016050	0.511851	−0.886552	−0.361933
C	12.000000	0.000000	0.000000	0.000000

[a] Given in parenthesis for each *j*. [b] Axes convention shown in Figure 1.

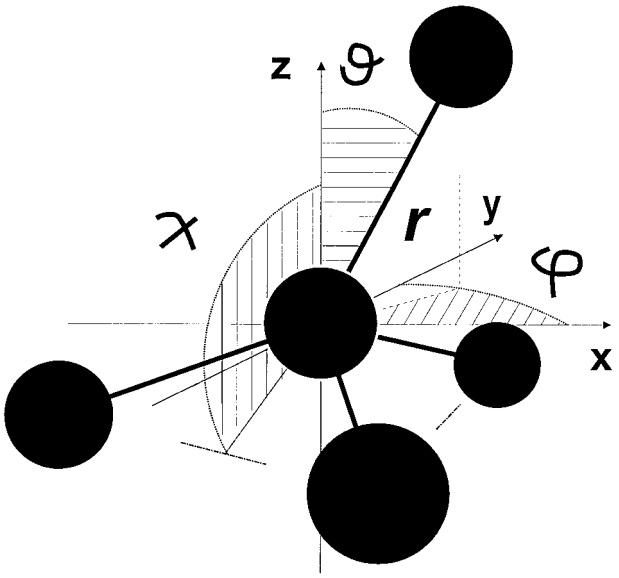

Figure 1. Internal "angular" coordinates and axes convention used to describe the wave packet dynamics of the CH chromophore in CHD_3, CHD_2T, and $CHDT_2$.

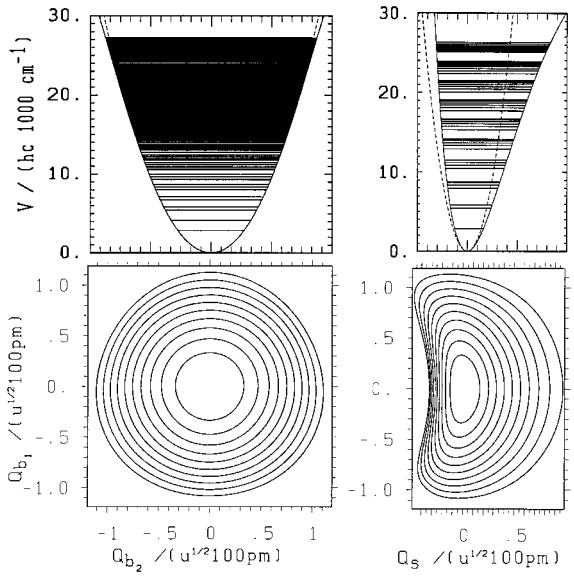

Figure 2. Potential energy cuts along the normal coordinate subspace pertaining to the CH chromophore in CHD_3. Q_{b_1} is an A' coordinate in C_s-symmetry, essentially changing structure along the *x*-axis in Figure 1, and Q_{b_2} is an A'' coordinate, essentially changing structure along the *y*-axis. Contour lines show equidistant energies at wave number differences of 3000 cm^{-1} up to correspondingly 30000 cm^{-1}. The upper curves are one-dimensional cuts along Q_{b_2} (left) and Q_s (right). The interrupted lines in the two upper figures show the corresponding harmonic potential curves.

which were finally used for the calculation of the energy on the nine-dimensional potential energy surface.

Sections of the potential energy surface along the normal coordinates are shown in Figure 2. The two-dimensional sections give an almost complete description of the chromophore potential up to energies corresponding to 30000 cm^{-1} (roughly 0.6 aJ; 1 aJ = 10^{-18} J). The equidistant contour lines are separated by 3000 cm^{-1}. The stretching−bending potential has a characteristic form related to the strong coupling which is at the origin of the Fermi resonance between the stretching and bending modes.[46]

The short-time dynamics of the CH chromophore in CHD_3 and other isotopomers of methane can be well described by this three-dimensional potential up to evolution times of 1 ps, probably even longer. From a first estimation of the high-resolution spectra for CHD_3,[46] we found that other modes are probably participating in the dynamics only at later times, which was also confirmed later,[62,63] for CHD_3 as well as for other related compounds.[64−68] Calculations of this effect using the global, full-dimensional potential surface of methane are currently being carried out in our laboratory.

The analytical, nine-dimensional vector valued dipole moment function was derived in refs 56 and 69 from an analysis of the electronic structure calculated ab initio and a direct adjustment to the experimental data for the overtone intensities of the CH chromophore in CHD_3. We used the following expression:

$$\hat{\mu}_k = \sum_{i=1}^{4} \frac{x_{i_k} - x_{5_k}}{r_i} \times \mu_b(r_i, \alpha_{ij}, \alpha_{ik}, \alpha_{il}) \qquad (5)$$

where μ_b is a generalized bond dipole function which depends on the bond lengths r_i and on the three neighboring valence bond angles α_{ij}, α_{ik}, α_{il} for *j*, *k*, $l \neq i$:

$$\mu_b(r_i, \alpha_{ij}, \alpha_{ik}, \alpha_{il}) = [\mu_b^0 + \mu_b^1(r_i - r_e) + \mu_b^2(r_i - r_e)^2 + \mu_b^3(r_i - r_e)^3 + \mu_a^1(\cos(\alpha_{ij}) + \cos(\alpha_{ik}) + \cos(\alpha_{il}) + 1) + \mu_a^2((2\cos(\alpha_{ij}) - \cos(\alpha_{ik}) - \cos(\alpha_{il}))^2 + 3(\cos(\alpha_{ik}) - \cos(\alpha_{il}))^2)] \times \exp(-\beta^2(r_i - r_e)^2) \quad (6)$$

The parameter values determined in ref 69 are $\mu_b^0 = 0.4$ D, $\mu_b^1 = -0.7$ D $Å^{-1}$, $\mu_b^2 = -0.7744$ D $Å^{-2}$, $\mu_b^3 = -0.1079$ D $Å^{-3}$, $\beta = 0.8922$ $Å^{-1}$, $\mu_a^1 = 0.0570$ D, $\mu_a^2 = 0.0243$ D, $r_e = 1.0858$ Å. The reduced dipole moment function in the subspace of the CH chromophore can be calculated in the same way as the reduced three-dimensional potential surface by calculation of cartesian coordinates (eq 2).

Equation 5 defines the components of the dipole moment vector in a molecule-fixed frame, such as that given by the *x*, *y*, and *z* axes in Figure 1, and the projections $x_{i_k} - x_{5_k}$ of the bond vectors onto these axes define the overall dipole moment in that direction. In our convention, μ_z leads to parallel-type transitions, μ_x and μ_y to perpendicular-type transitions of a symmetric top like CHD_3. μ_z and μ_x lead to transitions conserving the C_s symmetry of the equilibrium structure, μ_y leads

to transitions where this symmetry is broken and is thus adequate for the generation of dynamical chirality.

2.2. Calculations of Eigenstates and Effective Hamilton Matrix. The three-dimensional eigenstates (eigenfunctions $\phi_{N_i}(Q_s, Q_{b_1}, Q_{b_2})$ and eigenvalues E_{N_i}) were calculated with a discrete variable representation (DVR) technique in normal coordinates developed previously in our laboratory[59,60] (the nomenclature N_i will be explained below). The Hamiltonian is given by

$$\hat{H} = -\frac{h^2}{8\pi^2}\sum_{k=s,b_1,b_2}\left(\frac{\partial}{\partial Q_k}\right)^2 + V(Q_s, Q_{b_1}, Q_{b_2}) \qquad (7)$$

where h is Planck's constant. The relevant Hilbert subspace is spanned by product states

$$\chi_{i_s,i_{b_1},i_{b_2}}(Q_s, Q_{b_1}, Q_{b_2}) = \delta(Q_s - Q_{i_s}) \times \delta(Q_{b_1} - Q_{i_{b_1}}) \times \delta(Q_{b_2} - Q_{i_{b_2}}) \qquad (8)$$

where $\{Q_{i_x} \mid i_x = 1, ..., I_x\}$ is a grid of equidistant points in the normal coordinate manifold Q_x and $\delta(Q)$ is such that $\delta(Q - Q_0) = 0$, if $Q \neq Q_0$ and $\delta(Q - Q_0) = 1$, if $Q = Q_0$. The Hamiltonian is represented by the matrix $\boldsymbol{H}$ of rank $I_{3d} = I_s \times I_{b_1} \times I_{b_2}$, and was calculated with the matrix elements

$$\langle ijk \mid V \mid i'j'k'\rangle = \delta_{ii'}\delta_{jj'}\delta_{kk'}V(Q_{i_s}, Q_{j_{b_1}}, Q_{k_{b_2}}) \qquad (9)$$

$$\left\langle ijk \left| \frac{\partial}{\partial Q_s} \right| i'j'k' \right\rangle = \delta_{jj'}\delta_{kk'}\frac{\pi}{I_s\Delta_s}(-1)^{i-i'} \times \frac{1}{\sin\left(\pi\dfrac{i-i'}{I_s}\right)} \qquad (10)$$

I_s is the number of grid points along the stretching manifold, and Δ_s is the interval between them (analogous expressions hold for $\partial/\partial Q_{b_1}$ and $\partial/\partial Q_{b_2}$). The I_{3d} eigenvalues solve the equation

$$\boldsymbol{Z}^T\boldsymbol{H}\boldsymbol{Z} = \boldsymbol{Diag}(E_{0_1}, E_{(1/2)_1}, E_{(1/2)_2}, ...) \qquad (11)$$

where $\boldsymbol{Z}$ is the transformation matrix from the basis of product states to the eigenstates. The eigenfunctions are given by

$$\phi_{N_j}(Q_s, Q_{b_1}, Q_{b_2}) = \sum_k Z_{k;N_j}\chi_k(Q_s, Q_{b_1}, Q_{b_2}) \qquad (12)$$

where k is an index running over all product basis states in the column N_j of $\boldsymbol{Z}$. In the present calculations, effects from rotational motion and vibrational angular momentum couplings are neglected, since they are expected to be small compared with the vibrational couplings under investigation and are thus insignificant on the time scale of consideration here (however, the pseudopotential in Watson's hamiltonian was considered). Other effects from rotational motion will be discussed below.

Results for the eigenvalues of the three isotopomers CHD_3, CHD_2T and $CHDT_2$ are given in units of wave numbers in Table 2. These values can be described by an effective Hamilton matrix $\boldsymbol{H}^{eff}$. This matrix is defined for a general type CH chromophore within a C_s or C_1 environment[60] by the diagonal elements

$$H^{eff}_{v_s v_{b_1} v_{b_2}} = \tilde{\nu}'_s v_s + \tilde{\nu}'_{b_1} v_{b_1} + \tilde{\nu}'_{b_2} v_{b_2} + \tilde{x}'_{ss} v_s^2 + \tilde{x}'_{b_1 b_1} v_{b_1}^2 + \tilde{x}'_{b_2 b_2} v_{b_2}^2 + \tilde{x}'_{sb_1} v_s v_{b_1} + \tilde{x}'_{sb_2} v_s v_{b_2} + \tilde{x}'_{b_1 b_2} v_{b_1} v_{b_2} \qquad (13)$$

and off-diagonal elements

$$H^{eff}_{v_s,v_{b_1},v_{b_2};(v_s-1),(v_{b_1}+2),v_{b_2}} = k'_{sb_1b_1}\frac{1}{2}\sqrt{\frac{1}{2}v_s(v_{b_1}+1)(v_{b_1}+2)} \qquad (14)$$

$$H^{eff}_{v_s,v_{b_1},v_{b_2};(v_s-1),v_{b_1},(v_{b_2}+2)} = k'_{sb_2b_2}\frac{1}{2}\sqrt{\frac{1}{2}v_s(v_{b_2}+1)(v_{b_2}+2)} \qquad (15)$$

$$H^{eff}_{v_s,v_{b_1},v_{b_2};v_s,(v_{b_1}-2),(v_{b_2}+2)} = \gamma'\frac{1}{2}\sqrt{v_{b_1}(v_{b_1}-1)(v_{b_2}+1)(v_{b_2}+2)} \qquad (16)$$

$$H^{eff}_{v_s,v_{b_1},v_{b_2};(v_s-1),(v_{b_1}+1),(v_{b_2}+1)} = k'_{sb_1b_2}\frac{1}{2}\sqrt{\frac{1}{2}v_s(v_{b_1}+1)(v_{b_2}+1)} \qquad (17)$$

$\boldsymbol{H}^{eff}$ is block diagonal in the chromophore quantum number $N = v_s + (1/2)v_{b_1} + (1/2)v_{b_2}$. The quantities v_s, v_{b_1}, and v_{b_2} are stretching and bending vibrational quantum numbers. N may be an integer number, in which case there are $(N+1)^2$ diagonal elements in each matrix block, or N may be a half odd integer, with $(N + 1/2)(N + 3/2)$ diagonal elements. For CH chromophores in molecules of the type CHX_3 with C_{3v} symmetry, the bending vibrations are degenerate and one may transform the matrix to a representation with only one bending vibrational quantum number (v_b) and the quantum number l_b of the vibrational angular momentum,[46] which is approximately a good quantum number (see our discussion below).

The eigenstates within each block of the Hamilton matrix are denoted by N_j where the index j numbers states in order of decreasing energy. Their projection on configuration space is given by eq 12. These functions can similarly be written as

$$\phi_{N_j}(Q_s, Q_{b_1}, Q_{b_2}) = \sum_k Z^{eff}_{k;N_j}\chi^{eff}_k(Q_s, Q_{b_1}, Q_{b_2}) \qquad (18)$$

where k is now an index running over all *effective basis states.* $\boldsymbol{Z}^{eff}$ is the transformation matrix from the effective basis states to the eigenstates. The effective basis states form a set of zero-order states, which is different from the product basis states of eq 8. The nature of the corresponding wave functions can be revealed, for instance, by inverting the transformation eq 18, and inserting the result from eq 12 (here, we use the vector notation $\phi = (..., \phi_{N_j}, ...)^T$, $\boldsymbol{\chi} = (..., \chi_k, ...)^T$, $\boldsymbol{\chi}^{eff} = (..., \chi^{eff}_k, ...)^T$):

$$\boldsymbol{\chi}^{eff} = \mathbf{Z}^{eff^T}\phi \qquad (19)$$

$$= \mathbf{Z}^{eff^T}\mathbf{Z}\boldsymbol{\chi} \qquad (20)$$

$\mathbf{Z}^{eff^T}$ is the transposed matrix of $\mathbf{Z}^{eff}$. The calculation of effective basis functions from eq 20 is in principle straightforward. However, since the absolute phase of column vectors $\mathbf{Z}_{N_j} = (..., Z_{k;N_j}, ...)^T$ (and similarly $\mathbf{Z}^{eff}_{N_j}$) is undefined from the solution of the eigenvalue problem, there are many possible combinations of phases which lead to effective basis functions with the same spectrum and Hamilton matrix $\boldsymbol{H}^{eff}$. Since all matrix elements are real, possible phases are ± 1. We shall see, in Section 3, that some combinations may indeed lead to regularly structured effective basis functions which can have an interesting physical interpretation.

2.3. Calculation of Coherent Multiphoton Excitation. The vibrational excitation dynamics of molecules due to the absorp-

TABLE 2: Wave Numbers of the Overtone Spectrum of the CH Chromophore and Symmetry Classification for CHD_3, CHD_2T, and $CHDT_2$ (in cm^{-1})

			$\tilde{\nu}_{the}$					
N_j^a	$N_j^b\{l_b\}$	$\tilde{\nu}_{obs}$ (CHD_3)	CHD_3	$C_{3v}{}^c$	CHD_2T	C_s	CHT_2D	C_s
$(1/2)_2$	$(1/2)_1\{1\}$	1292.50 [96]	1307.666	*E*	1271.014	*A′*	1246.197	*A″*
$(1/2)_1$	$(1/2)_1\{1\}$	1292.50 [96]	1307.688	*E*	1305.412	*A″*	1288.487	*A′*
1_4	$1_2\{0\}$	2564.67 [46]	2595.546	A_1	2529.916	*A′*	2480.439	*A′*
1_3			2612.546	*E*	2573.649	*A″*	2532.555	*A″*
1_2			2612.634	*E*	2600.310	*A′*	2566.288	*A′*
1_1	$1_1\{0\}$	2992.75 [46]	2985.819	A_1	2984.868	*A′*	2984.02	*A′*
$(3/2)_6$	$(3/2)_2\{1\}$		3881.185	*E*	3778.036	*A′*	3703.701	*A″*
$(3/2)_5$	$(3/2)_2\{1\}$		3881.328	*E*	3827.066	*A″*	3762.483	*A′*
$(3/2)_4$			3914.978	*E*	3867.598	*A′*	3809.863	*A″*
$(3/2)_3$			3915.179	*E*	3885.948	*A″*	3834.494	*A′*
$(3/2)_2$	$(3/2)_1\{1\}$	4262.10 [46]	4266.217	*E*	4228.460	*A′*	4202.599	*A″*
$(3/2)_1$	$(3/2\ )_1\{1\}$	4262.10 [46]	4266.257	*E*	4262.696	*A″*	4244.738	*A′*
2_9	$2_3\{0\}$		5147.910	A_1	5015.761	*A′*	4916.298	*A′*
2_8			5164.781	*E*	5069.634	*A″*	4981.194	*A″*
2_7			5164.854	*E*	5113.872	*A′*	5034.318	*A′*
2_6			5215.260	*E*	5154.227	*A″*	5079.397	*A″*
2_5			5215.262	*E*	5164.357	*A′*	5094.730	*A′*
2_4	$2_2\{0\}$	5515.70 [46]	5527.112	A_1	5460.256	*A′*	5409.593	*A′*
2_3			5544.287	*E*	5503.828	*A″*	5461.436	*A″*
2_2			5544.317	*E*	5530.365	*A′*	5495.100	*A′*
2_1	$2_1\{0\}$	5864.98 [46]	5857.786	A_1	5855.193	*A′*	5852.914	*A′*
$(5/2)_{12}$	$(5/2)_3\{1\}$		6412.250	*E*	6243.273	*A′*	6118.351	*A″*
$(5/2)_{11}$	$(5/2)_3\{1\}$		6412.593	*E*	6301.043	*A″*	6188.736	*A′*
$(5/2)_{10}$			6445.844	*E*	6351.736	*A′*	6248.713	*A″*
$(5/2)_9$			6446.602	*E*	6388.444	*A″*	6294.584	*A′*
$(5/2)_8$			6513.350	*E*	6435.158	*A′*	6342.714	*A″*
$(5/2)_7$			6513.351	*E*	6439.033	*A″*	6349.954	*A′*
$(5/2)_6$	$(5/2)_2\{1\}$		6786.271	*E*	6681.702	*A′*	6606.041	*A″*
$(5/2)_5$	$(5/2)_2\{1\}$		6786.320	*E*	6730.542	*A″*	6664.515	*A′*
$(5/2)_4$			6820.228	*E*	6770.921	*A′*	6711.596	*A″*
$(5/2)_3$			6820.459	*E*	6789.201	*A″*	6736.246	*A′*
$(5/2)_2$	$(5/2)_1\{1\}$	7115.48 [46]	7111.831	*E*	7071.899	*A′*	7044.067	*A″*
$(5/2)_1$	$(5/2)_1\{1\}$	7115.48 [46]	7111.941	*E*	7106.254	*A″*	7086.440	*A′*
3_{16}	$3_4\{0\}$		7657.616	A_1	7460.538	*A′*	7309.853	*A′*
3_{15}			7674.557	*E*	7521.723	*A″*	7385.370	*A″*
3_{14}			7674.700	*E*	7576.368	*A′*	7450.642	*A′*
3_{13}			7725.454	*E*	7624.300	*A″*	7506.246	*A″*
3_{12}			7725.464	*E*	7649.759	*A′*	7541.434	*A′*
3_{11}			7809.499	*E*	7712.130	*A″*	7601.610	*A″*
3_{10}			7809.501	*E*	7713.086	*A′*	7603.974	*A′*
3_9	$3_3\{0\}$	8005.40 [46]	8026.664	A_1	7893.184	*A′*	7792.245	*A′*
3_8			8043.718	*E*	7946.833	*A″*	7856.824	*A″*
3_7			8043.803	*E*	7990.896	*A′*	7909.664	*A′*
3_6			8094.647	*E*	8031.134	*A″*	7954.348	*A″*
3_5			8094.648	*E*	8041.212	*A′*	7969.737	*A′*
3_4	$3_2\{0\}$	8347.10 [46]	8346.470	A_1	8277.083	*A′*	8224.013	*A′*
3_3			8364.152	*E*	8320.938	*A″*	8276.059	*A″*
3_2			8364.191	*E*	8347.509	*A′*	8309.947	*A′*
3_1	$3_1\{0\}$	8623.32 [46]	8616.279	A_1	8611.112	*A′*	8606.624	*A′*
$(7/2)_{20}$	$(7/2)_4\{1\}$		8899.868	*E*	8667.447	*A′*	8490.806	*A″*
$(7/2)_{19}$	$(7/2)_4\{1\}$		8900.459	*E*	8731.492	*A″*	8571.027	*A′*
$(7/2)_{18}$			8933.513	A_2	8790.372	*A′*	8641.457	*A″*
$(7/2)_{17}$			8935.267	A_1	8839.765	A″	8700.978	A′
$(7/2)_{16}$			9002.483	E	8888.049	A′	8754.319	A″
$(7/2)_{15}$			9002.485	E	8901.139	A″	8776.248	A′
$(7/2)_{14}$			9103.833	E	8986.529	A′	8857.719	A″
$(7/2)_{13}$			9103.833	E	8986.687	A″	8858.277	A′
$(7/2)_{12}$	$(7/2)_3\{1\}$		9265.009	E	9094.805	A′	8968.274	A″
$(7/2)_{11}$	$(7/2)_3\{1\}$		9265.240	E	9152.298	A″	9038.349	A′
$(7/2)_{10}$			9299.035	E	9202.818	A′	9097.997	A″
$(7/2)_9$			9299.881	E	9239.298	A″	9143.609	A′
$(7/2)_8$			9367.453	E	9286.074	A′	9191.198	A″
$(7/2)_7$			9367.454	E	9289.883	A″	9198.444	A′
$(7/2)_6$	$(7/2)_2\{1\}$		9579.937	E	9472.337	A′	9393.845	A″
$(7/2)_5$	$(7/2)_2\{1\}$		9579.990	E	9521.502	A″	9452.573	A′
$(7/2)_4$			9614.964	E	9562.153	A′	9499.767	A″
$(7/2)_3$			9615.242	E	9580.379	A″	9524.611	A′
$(7/2)_2$	$(7/2)_1\{1\}$	9852.76 [46]	9845.523	E	9801.733	A′	9770.708	A″
$(7/2)_1$	$(7/2)_1\{1\}$	9852.76 [46]	9845.721	E	9836.794	A″	9813.921	A′
4_{25}	$4_5\{0\}$		10122.546	A_1	9863.961	A′	9661.409	A′
4_{24}			10139.702	E	9930.250	A″	9745.730	A″

TABLE 2: (Continued)

			$\tilde{\nu}_{\text{the}}$					
N_j^a	$N_j^b\{l_b\}$	$\tilde{\nu}_{\text{obs}}$ (CHD_3)	CHD_3	C_{3v}	CHD_2T	C_s	CHT_2D	C_s
4_{23}			10139.959	E	9992.482	A′	9820.667	A′
4_{22}			10191.567	E	10048.190	A′	9886.065	A″
4_{21}			10191.595	E	10087.537	A″	9937.250	A′
4_{20}			10277.268	E	10144.874	A″	9994.551	A″
4_{19}			10277.279	E	10149.096	A′	10004.484	A′
4_{18}			10396.450	E	10259.076	A″	10112.054	A″
4_{17}			10396.450	E	10259.093	A′	10112.160	A′
4_{16}	$4_4\{0\}$		10484.001	A_1	10286.423	A′	10134.073	A′
4_{15}			10501.317	E	10347.225	A″	10209.232	A″
4_{14}			10501.481	E	10401.639	A′	10274.165	A′
4_{13}			10553.315	E	10449.466	A″	10329.389	A″
4_{12}			10553.323	E	10474.489	A′	10364.233	A′
4_{11}			10638.954	E	10537.479	A″	10423.911	A″
4_{10}			10638.956	E	10538.389	A′	10426.226	A′
4_9	$4_3\{0\}$		10794.426	A_1	10657.998	A′	10553.824	A′
4_8			10812.200	E	10712.033	A″	10618.743	A″
4_7			10812.302	E	10756.286	A′	10671.754	A′
4_6			10865.076	E	10796.981	A″	10716.441	A″
4_5			10865.077	E	10806.856	A′	10731.904	A′
4_4	$4_2\{0\}$	11063.60 [46]	11054.887	A_1	10981.039	A′	10923.954	A′
4_3			11073.999	E	11026.090	A″	10976.993	A″
4_2			11074.051	E	11052.973	A′	11011.505	A′
4_1	$4_1\{0\}$	11268.80 [46]	11262.393	A_1	11253.211	A′	11245.377	A′
⋮	⋮	⋮	⋮					
$(9/2)_2$	$(9/2)_1\{1\}$	12476.12 [97]	12469.865	E				
$(9/2)_1$	$(9/2)\{1\}$	12476.12 [97]	12470.177	E				
⋮		⋮	⋮	⋮				
5_4	$5_2\{0\}$	13664.68 [98]	13654.888	A_1				
5_1	$5_1\{0\}$	13799.35 [98]	13799.62	A_1				
⋮		⋮	⋮	⋮				
$(11/2)_6$	$(11/2)_2\{1\}$	14856.82 [97]	14840.618	E				
$(11/2)_5$	$(11/2)_2\{1\}$	14856.82 [97]	14840.855	E				
$(11/2)_2$	$(11/2)_1\{1\}$	14990.69 [97]	14992.413	E				
$(11/2)_1$	$(11/2)_1\{1\}$	14990.69 [97]	14992.884	E				
⋮		⋮	⋮	⋮				
6_4	$6_2\{0\}$	16156.91 [99]	16147.966	A_1				
6_1	$6_1\{0\}$	16230.67 [100]	16243.506	A_1				
⋮		⋮	⋮	⋮				
7_{13}	$7_3\{0\}$	18465.56 [99]	18465.56	A_l				
7_8	$7_2\{0\}$	18531.23 [99]	18528.95	A_l				

[a] N_j as defined in the text of the present work. [b] N_j as defined in ref 46 in the $C_{\infty v}$ approximation (the number in brackets gives the corresponding value of l_b). [c] The small deviations from equality in strictly degenerate levels in CHD_3 are due to round-off errors and mirror the expected quality of the calculations despite the quality of the convergence.

tion of coherent monochromatic infrared radiation can be described by the propagation of the vibrational wave function

$$\psi(t) = \sum_n b_n(t)\phi_n \tag{21}$$

In the present case, ϕ_n corresponds to the spectroscopic states ϕ_{N_j} from Section 2.2. The time-dependent coefficients $\mathbf{b}(t) = (..., b_n(t), ...)^T$ solve the time-dependent Schrödinger equation

$$i\frac{\mathrm{d}}{\mathrm{d}t}\mathbf{b}(t) = \{\boldsymbol{W} + f(t)\boldsymbol{V}^C\cos(\omega_L t)\}\,\mathbf{b}(t) \tag{22}$$

where

$$W_{nm} = \delta_{nm}\omega_n \tag{23}$$

(δ_{nm} is the Kronecker symbol) and the matrix elements

$$V_{nm}^C = -\left\langle \phi_n \left| \frac{2\pi}{h}\hat{\boldsymbol{\mu}}_f\cdot\mathbf{E_0} \right| \phi_m \right\rangle \tag{24}$$

give the coupling between the electric dipole moment vector $\hat{\boldsymbol{\mu}}_f$ and the electric field amplitude $\mathbf{E_0}$ of the linearly polarized coherent light. ω_n are the spectroscopic frequencies, given by $(2\pi E_{N_j})/h$ from Section 2.2, and the matrix elements in eq 24 can be calculated by summation on the grid of points defined in eq 8.

Equation 21 represents the time evolution of a quantized molecular system interacting with a classical electromagnetic field, described in eq 22 by a light pulse with carrier frequency ω_L and pulse shape function $f(t)$. In the present paper, $f(t)$ is a Heaviside unit step function, but it can in general be any other integrable function. The semiclassical approximation for the molecule−field interaction eq 22 is assumed to be valid, here, since the number of photons is very large at the intensities used for our calculations.

In eq 22 $\hat{\boldsymbol{\mu}}_f$ is the space-fixed dipole moment vector. For molecules in the gas phase, this vector changes orientation continuously. In order to discuss such effects as dynamical chirality, which are induced by an external, space-fixed field, the molecules need to be oriented with respect to the space-fixed coordinate system prior to the preparation and stay oriented during the probing of the internal, time-dependent structure. Such orientation schemes have received much attention recently, both experimentally and theoretically[70−73] (see also the review of Felker and Zewail in ref 74).

Oriented states can be described as superposition states of

several eigenstates of the angular momentum operator with different angular momentum quantum numbers. In the present as well as in our previous paper,[32] we neglect rotational states. The neglect of rotational states and its role on the excitation process is discussed below. However, this approximation can be used to represent the essence of the purely vibrational motion of molecules that are oriented in a space-fixed system and the assumption that it leads to a correct description of the vibrational wave packet motion was verified by full-dimensional quantum dynamical calculations of the wave packet motion of a diatomic molecule during excitation in an intense infrared field.[75] As long as the rotational motion is slow enough compared to the vibrational motion, we may choose the molecule-fixed and the space-fixed axes to coincide and neglect rotational states and reorientation aspects. Thus $\hat{\boldsymbol{\mu}}_f$ may be calculated directly from the expressions given in eq 5 above for $\hat{\boldsymbol{\mu}}$. Depending on the polarization axis of the electric field, the molecule can be excited along *x*, *y*, or *z* axes in Figure 1. Because of the large rotational constant of methane, the time scales on which an initially oriented state of the free molecule stays so are comparatively short and it would be also desirable to do calculations including rotational states explicitly. Such calculations were done early on for ozone at modest excitations,[76−78] but they would be quite difficult for the methane isotopomers at the high excitations considered here. Once feasible, they would provide interesting additional insights into rovibrational wave packet dynamics. An alternative would be to design electromagnetic fields that rotate with the molecule in space, semiclassically. In any case the present calculations should describe the main features of the short-time vibrational motion and going beyond this to include rovibrational motion will be difficult at present for methane. It should be made clear, however, that the present calculations are not meant to precisely model a particular real experimental situation for field-free, isolated methane molecules.

Solutions of eq 22 can be obtained by direct numerical integration. However, this can be very time consuming, when the number of coupled states becomes larger than 10. In the present paper, we are treating systems of roughly 1000 coupled states. In such situations, direct numerical integration becomes prohibitively expensive and, for long time propagations, presumably also quite inaccurate.[32] Equation 22 can also be solved by the Floquet (Liapunoff) method.[50,58,79,80] This method can also be time consuming for calculations with many coupled states, as in the present case. For treating the sequential multiphoton excitation of a many level system it is a good choice to use the quasiresonant approximation (QRA),[50,57,79,81] which is a good approximation if the coupling strength $|V_{ij}^C|$ and the resonance defects $X_k \equiv \omega_k - n_k\omega_L$ are both much smaller than the carrier excitation frequency ω_L (n_k is an appropriate integer, such that $|X_k| < \omega_L/2$). This approximation consists in solving the equation

$$i\frac{\mathrm{d}}{\mathrm{d}t}\mathbf{a}(t) = \left\{\boldsymbol{X} + \frac{1}{2}\boldsymbol{V}^{\mathrm{QRA}}\right\}\mathbf{a}(t) \tag{25}$$

where $\boldsymbol{X} = \boldsymbol{Diag}(..., X_k, ...)$, $V_{kj}^{\mathrm{QRA}} = V_{kj}^C$, if $|n_k - n_j| = 1$ and $V_{kj}^{\mathrm{QRA}} = 0$, if $|n_k - n_j| \neq 1$. The exact solution is then approximated by

$$\mathbf{b}(t) \approx \mathbf{b}^{\mathrm{QRA}}(t) = \mathbf{a}(t)\exp(-i \times n_k\omega_L t) \tag{26}$$

2.4. Rotational States. When rotational motion and excitation is also considered, a more general wave function $\Psi(t)$ must be used in eq 21, which depends on internal (vibrational) and rotational degrees of freedom.[76−78] In addition, the coupling operator in eq 22 acts on both rotational (through the direction cosine matrix $\hat{\boldsymbol{\lambda}}$—see Table I-1 in ref 82) and vibrational coordinates (through the molecule fixed dipole moment operator $\hat{\boldsymbol{\mu}}$):

$$\hat{\boldsymbol{\mu}}_f = \hat{\boldsymbol{\lambda}}\hat{\boldsymbol{\mu}} \tag{27}$$

Generally, inclusion of rotational degrees of freedom involves thus at least two aspects. First, the number of transitions (excitation channels) into the same vibrational level is increased. Since rotational level spacings are normally much smaller than vibrational level spacings, this leads to an increase of the effective coupling strength between vibrational levels at the same irradiation intensity. Alternatively, intensity can be reduced, when rotations are included, to achieve the same effective excitation as without rotations.[76−78]

A second, more relevant aspect for the discussion in the present paper involves the reorientation of the molecular frame with respect to the excitation field during the excitation process. In an adiabatic separation picture, one might think of a time-dependent effective coupling of vibrational states, induced by re-orientation, the time scale of which could be estimated from the change of expectation values $\langle\Psi(t)|\hat{\boldsymbol{\lambda}}|\Psi(t)\rangle$. Clearly, our assumption is that such changes occur on the time scale of rotational motion and are slower than the vibrational motion induced by the excitation at a given moment.

3. Results and Discussion

3.1. Potential Surfaces and Spectral Structure. At a first sight, the one-dimensional section of the potential surface along the out-of-plane CH bending normal coordinate in CHD_3, shown in Figure 2, is clearly less anharmonic than its one-dimensional stretching counterpart, also shown in that figure, even up to energies in the wave number region of 30000 cm^{-1}. Furthermore, the two-dimensional section in the CH bending subspace, spanned by the normal coordinates in the lower part of Figure 2, is approximately isotropic. This corresponds to an almost perfect $C_{\infty v}$ symmetry with respect to the azimuthal angle φ (see Figure 1), and is related to the approximate conservation for the bending vibration angular momentum l_b. While the first observation suggests that coherent multiphoton excitation of the CH bending manifold in CHD_3 might lead to a quasiclassical motion of the wave packet along that manifold,[51,52] which lives significantly longer than the motion induced along the stretching manifold under similar conditions,[32] the second observation suggests that the coupling among the bending manifolds is weak and raises the question to what extent such a weak coupling might lead to a motion of the wave packet with quasiclassical exchange of vibrational energy between the two bending manifolds, following paths which could be described by Lissajous figures of classical vibration mechanics, corresponding to CIVR.[32,53] Understanding quasiclassical exchange mechanisms of large-amplitude vibrational motion would clearly open one desirable route of controlling molecular vibrational motion and reaction dynamics.

The coherent excitation dynamics has been calculated with the spectroscopic data obtained with the methods described in Section 2. Details of the calculation are also described in that section. Wave numbers of spectroscopic states pertaining to the CH chromophore vibrations are collected in Table 2, together with experimental data from literature for comparison (a detailed discussion of the comparison is given in ref 83). We have included, as horizontal lines, the positions of these energies in the one-dimensional section $V(Q_{b_2})$ shown in Figure 2. These

lines correspond to a total number of 800 states up to 25000 cm^{-1}, which were all included in the present calculation of the dynamics. The energies of the spectroscopic states may be grouped into semi-isoenergetic shells defined by multiplets of states with constant chromophore quantum number *N*. These multiplets are also called polyads and can be well distinguished in the lower energy region, where the density of states is low. They are also distinguishable in the potential section $V(Q_s)$, on the right hand side of Figure 2, where we show only the subset of states with A_1 symmetry in the C_{3v} point group. This subset leads to parallel type bands and contains 105 states up to 20000 cm^{-1}, which were used in our previous work on the excitation dynamics along the stretching manifold. In order to test those results, we have reproduced them in the present work with the full set of states including perpendicular type bands, which will be discussed below.

Comparison of the calculated vibrational eigenvalues for CHD_3 with the known experimental values by means of Table 2 shows that the energetically highest states in a polyad are predicted almost always a few wave numbers lower than found experimentally, while the lower-lying states of a polyad are predicted systematically at slightly higher wave numbers than obtained experimentally. The calculated polyad structure is thus somewhat more compact than the experimental one. However, we expect no significant influence of this small difference on the time-dependent dynamics of the wave packet. The calculated *E* states of CHD_3 are not exactly degenerate, as should be expected, although the quality of the convergence with respect to the number of basis functions included has been extensively checked. The splitting is due to round-off errors which artificially break the symmetry. This is not significant for the wave packet evolution on short times considered here, as calculated splittings of about 0.02 to 0.2 cm^{-1} correspond to times of more than 0.1 to 1 ns.

At this point, we would like to draw the attention to the eigenstates of CHD_3 denoted as $(7/2)_{18}$ and $(7/2)_{17}$ at 8933.513 and 8935.267 cm^{-1} in Table 2. They are classified as A_2 and A_1 states, respectively, within the C_{3v} symmetry group. In case of an exact isotropic potential surface of CHD_3 with respect to the azimuthal angle φ (see Figure 1), these two states should be degenerate, with bending vibrational angular momentum $l_b = 3$ conserved. The small energy difference of 1.754 cm^{-1} between them is a demonstration of the anisotropy of the potential and the only approximate conservation of l_b. In ref 84, the influence of the anisotropy of the potential surface on the spectrum has been studied for model potentials of the CH chromophore in CHD_3, which are functions of the Q_b and Q_s normal coordinates. In order to quantify the deviation from an isotropic potential, an anisotropy parameter as defined in ref 84 has been introduced. Comparison of the above energy difference with the results for the corresponding eigenstates in ref 84 implies that an anisotropy parameter of roughly -1000 cm^{-1} is expected, if the potential surface used here, which is a function of bond lengths and angles, is expressed as a function of Q_b and Q_s similar to the model potentials studied in ref 84.

The structure of the molecular eigenfunctions ϕ_i (eq 12) is very similar to that shown in ref 46 and will be addressed in our discussion of effective basis functions from eq 20 below. In Table 3 we list also some of the transition matrix elements $\mu_{ij}(\alpha) = \langle\phi_i|\ \hat{\mu}_\alpha|\phi_j\rangle$ (α is one direction in a molecule-fixed frame), which are important for the sequential infrared multiphoton excitation.

3.2. Population Dynamics. Coherent multiphoton excitation of the bending motion is efficient with a carrier frequency in the region of the bending fundamentals. Classically, this corresponds to forcing the oscillators to oscillate resonantly at their own frequencies. Figure 3 shows the time evolution of populations

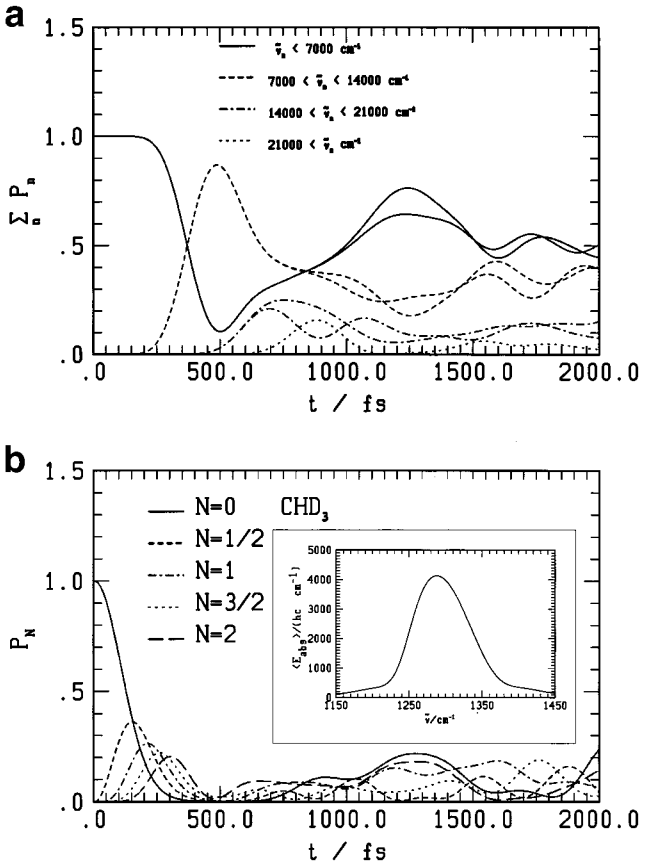

Figure 3. Time evolution of coarse grained level populations of the CH chromophore in CHD_3 during excitation along the *y*-axis (see Figure 1) with a laser tuned at 1300 cm^{-1} and an intensity of 10 TW cm^{-2}. (a) Coarse grained populations $\Sigma_n p_n(t)$, for states with wave numbers $\tilde{\nu}_n$ falling in the regions below 7000 cm^{-1} (solid continuous line), 7000 and 14000 cm^{-1} (interrupted line), 14000 and 21000 cm^{-1} (solid-dotted interrupted line) and above 21000 cm^{-1} (dotted line); (b) coarse grained populations $p_N(t) = \Sigma_j p_{N_j}(t)$ of levels of semi-isoenergetic states defined by the chromophore quantum number *N* (see text). The insert shows the time averaged absorbed energy spectrum after 500 fs, as calculated with eq 29.

$$p_n(t) = b_n(t)^* b_n(t) \tag{28}$$

of CH polyad eigenstates in CHD_3 (the index *n* stands for any of the states N_j) during the excitation with a carrier frequency corresponding to $\tilde{\nu}_L = 1300$ cm^{-1} and an intensity $I_0 = 10$ TW cm^{-2}. The pulse shape function is rectangular, which means that for pulses long enough the calculations can be used to simulate the excitation with a CW laser. Initially, the system is in the vibrational ground state and the molecule is assumed to be oriented such that the electric field is parallel to the *y*-axis. In Figure 3a, the curves show the total population of states $\Sigma_n p_n(t)$ which fall in certain wave number intervals as indicated in the figure. We see that considerable excitation of states above 7000 cm^{-1} sets in after 200 fs, and above 14000 cm^{-1} after nearly 500 fs at these conditions. As a check of convergence, each curve was calculated twice: For a system containing 800 states up to 25000 cm^{-1}, as shown in Figure 2, and for a smaller system with nearly 600 states up to 21000 cm^{-1}. The two sets of curves are identical on the scale of the figure in the first 500

TABLE 3: Electric Dipole Matrix Elements[a] for CHD_3, CHD_2T, and $CHDT_2$ (in Debye)

		$\langle N_j\|\mu_\alpha\\|N'_j\rangle_{the}$/Debye[a]								
		CHD_3			CHD_2T			$CHDT_2$		
N_j	N'_j	$\alpha = x$	$\alpha = y$	$\alpha = z$	$\alpha = x$	$\alpha = y$	$\alpha = z$	$\alpha = x$	$\alpha = y$	$\alpha = z$
0_1	$(1/2)_2$	-0.4863×10^{-1}			-0.5078×10^{-1}				0.5454×10^{-1}	
0_1	$(1/2)_1$		-0.4863×10^{-1}			-0.5154×10^{-1}		0.5299×10^{-1}		-0.9173×10^{-2}
0_1	1_4			-0.7849×10^{-2}	0.3388×10^{-3}		-0.5331×10^{-2}	-0.8497×10^{-3}		0.4811×10^{-2}
0_1	1_3		0.1079×10^{-2}			-0.1461×10^{-2}			0.1026×10^{-2}	
0_1	1_2	-0.1080×10^{-2}		-0.1539×10^{-4}	0.8356×10^{-3}			-0.1265×10^{-2}		0.4690×10^{-2}
0_1	1_1			-0.5325×10^{-1}	0.4097×10^{-3}		-0.5312×10^{-1}	-0.3977×10^{-3}		-0.5297×10^{-1}
$(1/2)_2$	1_4	0.4981×10^{-1}			0.7216×10^{-1}		0.1512×10^{-1}		-0.7757×10^{-1}	
$(1/2)_2$	1_3	-0.4886×10^{-1}				0.5165×10^{-1}		0.5318×10^{-1}		-0.9010×10^{-2}
$(1/2)_2$	1_2	-0.4872×10^{-1}		0.2445×10^{-3}	0.8517×10^{-2}		0.1858×10^{-2}		0.8583×10^{-3}	
$(1/2)_2$	1_1	0.1013×10^{-2}			-0.4770×10^{-3}		-0.1406×10^{-2}		0.8582×10^{-3}	
$(1/2)_1$	1_4		0.4954×10^{-1}			0.9750×10^{-2}		-0.8489×10^{-2}		0.1202×10^{-2}
$(1/2)_1$	1_3	-0.4886×10^{-1}		-0.2430×10^{-3}	0.5104×10^{-1}		0.1112×10^{-1}		0.5477×10^{-1}	
$(1/2)_1$	1_2		0.4900×10^{-1}			-0.7299×10^{-1}		0.7531×10^{-1}		-0.1295×10^{-1}
$(1/2)_1$	1_1		0.1003×10^{-2}			-0.1582×10^{-2}		0.1363×10^{-2}		-0.1248×10^{-2}
1_4	$(3/2)_6$	0.7052×10^{-1}			0.8909×10^{-1}		0.1825×10^{-1}		0.9570×10^{-1}	
1_4	$(3/2)_5$		0.7032×10^{-1}			0.5266×10^{-1}		0.5396×10^{-1}		-0.8949×10^{-2}
1_4	$(3/2)_4$				0.8117×10^{-2}		0.1657×10^{-2}		0.7624×10^{-2}	
1_4	$(3/2)_3$				0.7979×10^{-4}		-0.5620×10^{-3}	0.2069×10^{-2}		-0.2851×10^{-3}
1_4	$(3/2)_2$		-0.1701×10^{-2}			0.2623×10^{-2}			-0.1706×10^{-2}	
1_4	$(3/2)_1$	0.7113×10^{-2}			0.1209×10^{-2}		0.1933×10^{-2}	-0.5219×10^{-3}		0.1572×10^{-3}
1_4	2_9	-0.2129×10^{-4}		0.1591×10^{-1}	0.1198×10^{-2}		-0.1244×10^{-1}	-0.2105×10^{-2}		-0.1124×10^{-1}
1_4	2_8		0.1902×10^{-2}			-0.2296×10^{-2}			-0.1822×10^{-2}	
1_4	2_7	0.1903×10^{-2}		0.1096×10^{-3}	0.9870×10^{-3}		0.4025×10^{-2}	-0.1374×10^{-2}		0.3859×10^{-2}
1_4	2_6	0.1320×10^{-3}		-0.1204×10^{-4}		-0.4475×10^{-3}			0.3396×10^{-3}	
1_4	2_5		-0.1289×10^{-3}		0.2067×10^{-3}		0.5463×10^{-3}	-0.2157×10^{-3}		0.4221×10^{-3}
1_4	2_4			0.5276×10^{-1}	0.4446×10^{-3}		-0.5297×10^{-1}	-0.3084×10^{-3}		-0.5293×10^{-1}
1_4	2_3		-0.1490×10^{-4}			-0.3111×10^{-4}			-0.7747×10^{-5}	
1_4	2_2	0.1399×10^{-4}		-0.1628×10^{-3}			0.2955×10^{-4}	-0.1543×10^{-4}		-0.4480×10^{-4}
1_4	2_1			0.7132×10^{-3}	-0.3956×10^{-4}		0.3621×10^{-3}	0.2760×10^{-4}		0.2412×10^{-3}
1_3	$(3/2)_6$		-0.3573×10^{-1}			0.1347×10^{-1}		-0.1200×10^{-1}		0.1603×10^{-2}
1_3	$(3/2)_5$	-0.3596×10^{-1}		-0.3097×10^{-3}	0.7063×10^{-1}		0.1496×10^{-1}		-0.7649×10^{-1}	
1_3	$(3/2)_4$	-0.6000×10^{-1}				-0.7261×10^{-1}		0.7505×10^{-1}		-0.1269×10^{-1}
1_3	$(3/2)_3$		0.6012×10^{-1}		0.1831×10^{-1}		0.4028×10^{-2}		-0.1628×10^{-1}	
1_3	$(3/2)_2$	0.1211×10^{-2}		0.7399×10^{-4}		0.1790×10^{-2}		0.1547×10^{-2}		-0.1211×10^{-2}
1_3	$(3/2)_1$		-0.1199×10^{-2}		0.6035×10^{-3}		0.1450×10^{-2}		0.9894×10^{-3}	
1_3	2_9		-0.1127×10^{-2}			-0.5078×10^{-3}			0.4017×10^{-3}	
1_3	2_8	-0.4850×10^{-4}		-0.1375×10^{-1}	0.4106×10^{-3}		-0.1079×10^{-1}	-0.1133×10^{-2}		-0.9607×10^{-2}
1_3	2_7		-0.6651×10^{-4}			0.2420×10^{-2}			-0.1892×10^{-2}	
1_3	2_6		-0.1852×10^{-2}		0.1522×10^{-2}		0.6789×10^{-2}	-0.2258×10^{-2}		0.6578×10^{-2}
1_3	2_5	0.1853×10^{-2}		0.7582×10^{-4}		0.1263×10^{-2}			-0.7915×10^{-3}	
1_3	2_4		-0.1059×10^{-4}			0.1074×10^{-3}			-0.1222×10^{-3}	
1_3	2_3	-0.1617×10^{-4}		0.5273×10^{-1}	0.4867×10^{-3}		-0.5277×10^{-1}	-0.4100×10^{-3}		-0.5277×10^{-1}
1_3	2_2		0.1761×10^{-4}			-0.4631×10^{-4}			0.2332×10^{-4}	
1_3	2_1		-0.3122×10^{-4}			0.2115×10^{-4}			-0.1334×10^{-4}	
1_2	$(3/2)_6$	-0.3569×10^{-1}		0.3102×10^{-3}	0.2480×10^{-2}		0.3647×10^{-3}		0.2056×10^{-2}	
1_2	$(3/2)_5$		0.3585×10^{-1}			-0.1828×10^{-1}		-0.1566×10^{-1}		0.2353×10^{-2}
1_2	$(3/2)_4$		-0.6018×10^{-1}		0.5192×10^{-1}		0.1142×10^{-1}		0.5546×10^{-1}	
1_2	$(3/2)_3$	-0.6003×10^{-1}				0.8872×10^{-1}		0.9201×10^{-1}		-0.1574×10^{-1}
1_2	$(3/2)_2$		-0.1208×10^{-2}		-0.2423×10^{-3}		0.1934×10^{-3}		0.1834×10^{-3}	
1_2	$(3/2)_1$	-0.1207×10^{-2}		0.7968×10^{-4}		-0.2822×10^{-2}		0.2444×10^{-2}		-0.1787×10^{-2}
1_2	2_9	0.1126×10^{-2}		-0.8955×10^{-4}	0.1216×10^{-3}		-0.1583×10^{-3}	-0.9941×10^{-4}		-0.1288×10^{-3}
1_2	2_8		0.5339×10^{-4}			0.4725×10^{-3}			-0.3299×10^{-3}	
1_2	2_7	-0.3919×10^{-4}		0.1375×10^{-1}	-0.3410×10^{-3}		-0.9993×10^{-2}	-0.8568×10^{-4}		-0.8372×10^{-2}
1_2	2_6	-0.1853×10^{-2}		0.4296×10^{-4}		-0.2426×10^{-2}			0.1735×10^{-2}	

TABLE 3: (Continued)

		$\langle N_j\|\mu_\alpha\|N'_j\rangle_{the}$/Debye[a]									
		CHD_3			CHD_2T			$CHDT_2$			
N_j	N'_j	$\alpha = x$	$\alpha = y$	$\alpha = z$	$\alpha = x$	$\alpha = y$	$\alpha = z$	$\alpha = x$	$\alpha = y$	$\alpha = z$
1_2	2_5		-0.1853×10^{-2}		0.1817×10^{-2}		0.1044×10^{-1}	-0.2843×10^{-2}		0.1022×10^{-1}
1_2	2_4			0.1661×10^{-3}			-0.2627×10^{-4}	0.1118×10^{-4}		-0.6631×10^{-4}
1_2	2_3		0.1811×10^{-4}			-0.1372×10^{-3}			0.1110×10^{-3}	
1_2	2_2	0.1950×10^{-4}		0.5272×10^{-1}	-0.4816×10^{-3}		0.5260×10^{-1}	0.5194×10^{-3}		0.5266×10^{-1}
1_2	2_1	0.3108×10^{-4}					-0.4410×10^{-3}			-0.3570×10^{-3}
1_1	$(3/2)_6$	0.4799×10^{-3}			-0.4049×10^{-3}		0.1021×10^{-3}		-0.3981×10^{-3}	
1_1	$(3/2)_5$		0.4752×10^{-3}			-0.3264×10^{-3}		-0.2882×10^{-3}		-0.8849×10^{-4}
1_1	$(3/2)_4$				0.1612×10^{-3}		0.3521×10^{-4}		0.1562×10^{-3}	
1_1	$(3/2)_3$			-0.1019×10^{-3}		0.3289×10^{-3}		0.3220×10^{-3}		0.1359×10^{-4}
1_1	$(3/2)_2$		-0.4534×10^{-1}		-0.4737×10^{-1}		-0.1101×10^{-1}		0.5105×10^{-1}	
1_1	$(3/2)_1$	0.4534×10^{-1}				-0.4822×10^{-1}		0.4973×10^{-1}		-0.9253×10^{-2}
1_1	2_9			-0.3827×10^{-3}	-0.3245×10^{-4}		-0.2152×10^{-3}			-0.1903×10^{-3}
1_1	2_8					-0.2984×10^{-4}			-0.1015×10^{-4}	
1_1	2_7						0.2143×10^{-3}	-0.2938×10^{-4}		0.1853×10^{-3}
1_1	2_6	0.2532×10^{-4}							-0.1043×10^{-4}	
1_1	2_5		-0.2524×10^{-4}		-0.1655×10^{-4}		-0.1470×10^{-3}	0.1988×10^{-4}		-0.1371×10^{-3}
1_1	2_4			-0.1064×10^{-1}	0.3669×10^{-3}		-0.7057×10^{-2}	-0.8361×10^{-3}		-0.6310×10^{-2}
1_1	2_3		0.1043×10^{-2}			-0.1392×10^{-2}			0.1033×10^{-2}	
1_1	2_2	-0.1043×10^{-2}		0.1644×10^{-4}	-0.8242×10^{-3}		-0.6782×10^{-2}	0.1200×10^{-2}		-0.6260×10^{-2}
1_1	2_1			0.8051×10^{-1}	0.4416×10^{-3}		-0.8040×10^{-1}	-0.4472×10^{-3}		-0.8025×10^{-1}

[a] Matrix elements smaller than 10^{-5} Debye are omitted.

fs of excitation, and start bifurcating at 600−700 fs, from which we conclude that calculations are converged, under the given conditions and for the purposes of the present work, during the first 600 fs of excitation. We expect the evolution to be qualitatively correct also at later times shown in the figure.

If we use, for the bending excitation, the same irradiation intensity as for the stretching excitation in our previous work ($I_0 = 30$ TW cm^{-2}), the uppermost states at 25000 cm^{-1} are already significantly populated after the first 300 fs of excitation, which disables converged calculations at that intensity for later times. However, calculations in our previous work were fully converged. This shows that coherent excitation along the bending manifolds (either *x*- or *y*-axis) is indeed much more efficient than excitation along the stretching manifold at similar conditions. There are at least two reasons for this: first, the bending potentials are less anharmonic and the resonance defects X_k of bending states (cf. eq 25) increase at a somewhat lower rate with energy than for stretching states; secondly, the effective density of near resonant states for the sequential multiphoton process is obviously much larger for the bending than for the stretching manifolds, as shown in Figure 2. Bending excitation may be expected to be more efficient than stretching excitation even when rovibrational transitions are considered.

In Figure 3b we show the time evolution of populations $p_N = \Sigma_j p_{N_j}$ for the values $N = 0$, 1/2, 1, 3/2, and 2 of the chromophore quantum number. We also show in this figure the short-time absorption spectrum

$$\langle E\rangle_T = \frac{1}{T}\int_0^T E(t)\mathrm{d}t \tag{29}$$

as a function of the irradiation wave number, where $T \approx 500$ fs and

$$E(t) = \sum_j (p_j(t) - p_j(0))E_j \tag{30}$$

is the absorbed energy. The short time used is imposed by the convergence limit of our calculations and the result is a broad spectrum with a maximum near 1300 cm^{-1}, which is related to the position of the spectroscopic states in Table 2 and explains the preference for the chosen carrier wave number for the excitation process in this example under the given conditions.

The populations p_N correspond to level populations of polyads which are nearly resonant with multiples of the bending harmonic wave number. As shown in the figure, the initial time evolution of populations is indeed very similar to that of a driven one-dimensional harmonic oscillator.[52] This behavior was found for the stretching excitation[32] only in the initial 50 fs of excitation, for the sequence of even chromophore quantum numbers $N = 0$, 1, 2, ..., which correspond to multiples of the stretching harmonic wave number. From this result we could conclude that the bending motion might indeed be quasiclassical for substantially longer times than the stretching motion, at least during the initial 500 fs of excitation. However, before drawing final conclusions, the motion of the wave packet in configuration space must also be investigated.

For symmetric tops like CHD_3 one might expect the bending excitation along the *x*-axis to be a similar process. The question is, whether such processes can be distinguished and, if yes, how can this be used for the purpose of guiding nuclear motion along different directions in the molecule-fixed frame. While the theoretical treatment of such questions might have a direct bearing on experiments where molecules have well-defined orientations, for instance on surfaces[85] or in external fields,[86] it

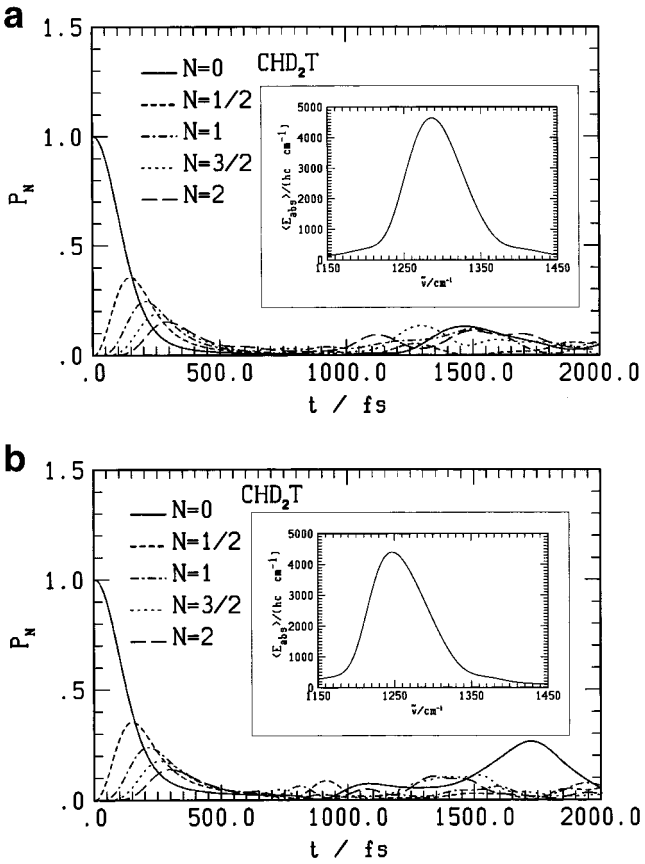

Figure 4. Time evolution of coarse grained level populations $p_N(t) = \Sigma_j p_{N_j}(t)$ of the CH chromophore in CHD_2T during excitation with an intensity of 10 TW cm^{-2}. (a) Excitation along the *y*-axis (laser tuned at 1270 cm^{-1}); (b) excitation along the *x*-axis (laser tuned at 1230 cm^{-1}). The insert in each figure shows the time averaged absorbed energy spectrum after 500 fs for the corresponding excitation, as calculated with eq 29.

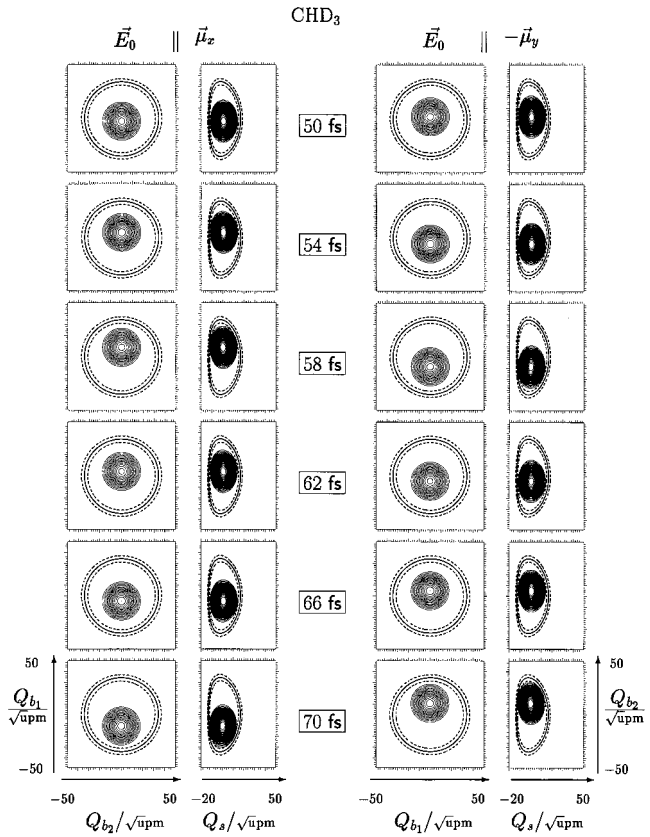

Figure 5. Snapshots of the time evolution of reduced two-dimensional probability densities $|\psi_{bb}|^2$ and $|\psi_{sb}|^2$ (see eqs 32 and 31, respectively), for the excitation of CHD_3 under the same conditions as discussed above in Figure 3, between 50 and 70 fs. The dark solid curve is a cut of the potential energy surface at the currently absorbed energy eq 30, which is roughly constant and corresponds to 3000 cm^{-1} during the time interval shown here (≈6000 cm^{-1}, if zero-point energy is included). The dark dotted curves show the energy uncertainty eq 33 of the time-dependent wave packet, approximately 500 cm^{-1} in the present case. (Left-hand side) Excitation along the *x*-axis. The vertical axis in the two-dimensional contour line representations is the Q_{b_1}-axis, the horizontal axes are Q_{b_2} and Q_s, for $|\psi_{bb}|^2$ and $|\psi_{sb}|^2$, respectively. (Right-hand side) Excitation along the *y*-axis, but with the field vector pointing into the negative *y*-axis. In the two-dimensional contour line representations, the vertical axis is the Q_{b_2}-axis, the horizontal axes are Q_{b_1} and Q_s, for $|\psi_{bb}|^2$ and $|\psi_{sb}|^2$, respectively. The lowest contour line has the value 44×10^{-5} u^{-1} pm^{-2}, the distance between them is 7×10^{-5} u^{-1} pm^{-2}. Maximal values are nearly constant for all snapshots in this figure, and correspond to 140×10^{-5} u^{-1} pm^{-2} for $|\psi_{bb}|^2$ and 180×10^{-5} u^{-1} pm^{-2} for $|\psi_{sb}|^2$.

is certainly more complex for gas-phase experiments, when rotations of the molecules must be considered in addition to the internal vibrational motion, as discussed in Section 2. Discrimination between the molecule-fixed axes require pre-orientation along the appropriate axis before the excitation process takes place. Such experiments have become feasible in the gas phase with techniques from time-resolved spectroscopy on the femtosecond time scale (see, for example, the review of Felker and Zewail[74]).

For asymmetric tops with significantly different frequencies of vibrational motion along selected axes, discrimination might be efficient without pre-orientation by choosing the excitation irradiation in the corresponding wave number region of the vibration of interest. Figure 4 shows the time evolution of polyad populations in the case of CHD_2T at an intensity of 10 TW cm^{-2} along the *y*-axis (Figure 4a), with the laser tuned at 1270 cm^{-1}, and along the *x*-axis (Figure 4b), with the laser at 1230 cm^{-1}. We also show the short-time absorption spectrum as defined in eq 29, which explains the choice of these carrier wave numbers at the maximum absorption position. The discrimination of axes is not apparent from observation of the time evolution of polyad populations. However, in a high-resolution experiment one would probably observe differences in the time evolution of single states within one polyad. In the next section we shall discuss the difference of wave packet motion between excitation along the *x*- and *y*-axes.

3.3. Wave Packet Motion. The wave packet motion of the CH chromophore is represented by snapshots of the time-dependent probability density distribution $|\psi(t, Q_s, Q_{b_1}, Q_{b_2})|^2$, where the probability amplitude ψ is defined in eq 21 as an expansion in the basis of spectroscopic states, which in turn were defined by eq 12. More specifically, and for practical purposes, we show simultaneous two-dimensional representations

$$|\psi_{sb}(t, Q_s, Q_{b_i})|^2 = \int_{Q_{b_j}} \mathrm{d}Q_{b_j} |\psi(t, Q_s, Q_{b_i}, Q_{b_j})|^2 \; (\mathrm{i} \neq j) \quad (31)$$

and

$$|\psi_{bb}(t, Q_{b_1}, Q_{b_2})|^2 = \int_{Q_s} \mathrm{d}Q_s |\psi(t, Q_s, Q_{b_1}, Q_{b_2})|^2 \quad (32)$$

Such a sequence of snapshots, calculated in intervals of 4 fs, is shown as a series of contour line plots on the left-hand side of Figure 5; the outermost column shows the evolution of $|\psi_{bb}(t, Q_{b_2}, Q_{b_1})|^2$, the innermost column is $|\psi_{sb}(t, Q_s, Q_{b_1})|^2$ at the same

time steps. This is the wave packet motion in CHD_3 for excitation with a linearly polarized field along the *x*-axis at 1300 cm^{-1} and 10 TW cm^{-2} after 50 fs of excitation.

In our convention, nuclear displacements along Q_{b_1} occur along the *x*-axis, displacements along Q_{b_2} are directed along the *y*-axis. One observes a semiclassical, nearly periodic motion of the wave packet along the excited manifold with a period of approximately 24 fs, corresponding to the frequency of CH bending vibrations in the wave number region around 1500 cm^{-1}. At this stage of the excitation process, the motion of the wave packet is essentially one dimensional, as seen from the trajectory followed by the maximum of the probability distribution and its practically unchanged shape during the forth and back oscillations between the turning points. The latter lie on the potential energy section defined by the actual energy $E(t)$ of the wave packet, which is defined in eq 30, and describes the classically accessible region in configuration space. These potential energy sections are shown by the continuous curves in the figures, which are surrounded by dotted curves describing the energy uncertainty

$$\Delta E(t) = \sqrt{\sum_j p_j(t)(E_j - E(t))^2} \qquad (33)$$

of the wave packet (see legend to Figure 5 for values).

The sequence on the right hand side of Figure 5 shows wave packets $|\psi_{bb}(t, Q_{b_1}, Q_{b_2})|^2$ and $|\psi_{sb}(t, Q_s, Q_{b_2})|^2$ during the excitation along the *y*-axis. Here, we have chosen to excite antiparallel to the *y*-axis ($\mathbf{E_0} \parallel -\boldsymbol{\mu}_y$). We can see that this choice induces a phase shift of π between the two wave packets shown in the figure, in addition to forcing oscillations along different directions.

Figure 6 shows the continuation of the wave packet motion at later times. We can still recognize an approximately oscillatory behavior along the excitation manifold (Q_{b_1} or *x*-axis on the left-hand side, Q_{b_2} or *y*-axis on the right-hand side). On top of this, there is now also an alternating squeezing and spreading of the wave packet. During the spreading, it covers much of the second bending manifold, which has not initially been excited. This covering is not complete. However, the motion of the wave packet in the bending manifold (bending−bending representation) is clearly not of the simple Lissajous type. In the stretching−bending representation, the shape of the wave packet changes less, although the creation of ripples can be observed at some times, and we can say that the center-of-mass of the wave packet moves essentially along the path of least action, as for a classical motion. The initially induced phase shifts along the different excitation directions prevail up to this stage. The energy values in Figure 6 are $\langle E(t)/hc\rangle \approx 12700$ cm^{-1} (for all snapshots; including zero-point energy) and $\Delta E(t)/hc \approx 2200$ cm^{-1}.

For the asymmetric top CHD_2T we initially also observe a semiclassical wave packet motion of the CH chromophore which is very similar to that in CHD_3 shown in Figure 5, including a π phase shift induced by antiparallel excitation along the *y*-axis, and we will not reproduce this result here. Differences become evident when vibrational redistribution processes had time to set in, typically after 100 to 200 fs. This is shown in the series of snapshots in Figure 7. Excitation conditions are basically the same as for CHD_3, apart for the excitation wave number, which is 1230 cm^{-1} here, for excitation along the *x*-axis, and 1270 cm^{-1}, for excitation along the *y*-axis, corresponding to the maximum positions in Figure 4. The energy values in Figure 7 are $\langle E(t)/hc\rangle \approx 12500$ cm^{-1} (zero-point energy included) and

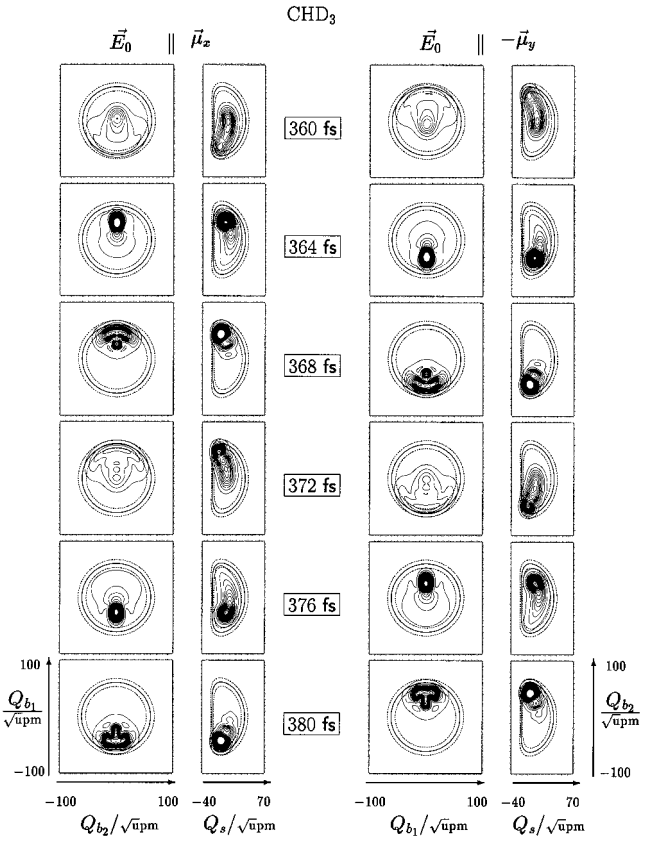

Figure 6. Snapshots of the time evolution of reduced two-dimensional probability densities during the excitation of CHD_3 under the same conditions as in Figure 5 (see also the legend to that figure), but for a time interval between 360 and 380 fs. The absorbed energy corresponds to 9700 cm^{-1} (starting from the zero-point level), the uncertainty to 2200 cm^{-1}. The lowest contour line has the value 4×10^{-5} u^{-1} pm^{-2}, the distance between them is 7×10^{-5} u^{-1} pm^{-2}. Maximal values are variable according to the number of contour lines shown.

$\Delta E(t)/hc \approx 3800$ cm^{-1}. The motion of the wave packet is still oscillatory, as before. However, the superposed squeezing and spreading of the wave packet is much stronger for the excitation along the *y*-axis than for the *x*-axis. Excitation along the *y*-axis leads to a significantly larger, delocalized occupation of the not directly excited *x*-manifold, while the inverse is not true. This distinction of wave packet motion is absent in the case of CHD_3, where excitation along any of the axes leads to delocalization of the wave packet after some typical time. A second difference is that the π phase shift between the *x* and *y* excitation, which we invoked initially by antiparallel excitation, has vanished at this stage of the dynamics.

Spreading of probability density becomes even more evident after 500 fs of excitation (Figure 8), when it is replacing oscillatory motion due to DIVR.[32] The probability distribution starts to fill the energetically accessible region, with exception of the bending−bending representation during *x*-axis excitation. The wave packet motion seems thus to be confined to the $\{Q_s, Q_{b_1}\}$ subspace after excitation along the *x*-axis. However, a closer inspection of the figure suggests that leaking out of probability density into the Q_{b_2}-manifold might start at later times from those regions of configuration space where $|Q_{b_1}|$ is maximal. In Figure 8, $\langle E(t)/hc\rangle \approx 16300$ cm^{-1}, including zero-point energy (for all snapshots), and $\Delta E(t)/hc \approx 4800$ cm^{-1}.

These results can be understood partly after inspection of atomic displacements during the motion, described by the ***l*** matrix in Table 1, CHD_2T. We assume that redistribution processes are likely to be more efficient at larger displacements

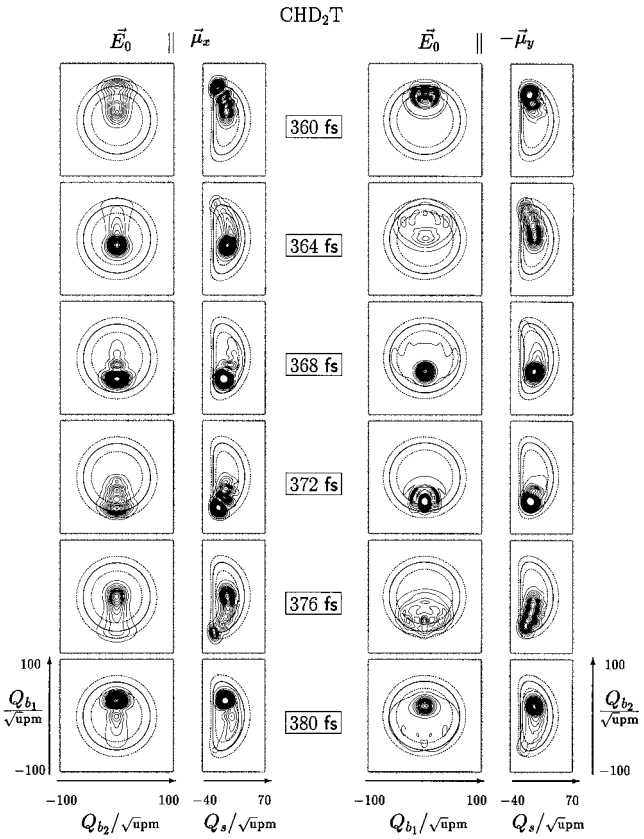

Figure 7. Snapshots of the time evolution of reduced two-dimensional probability densities during the excitation of CHD_2T under the same conditions as in Figure 4 (see also the legend to Figure 5), for a time interval between 360 and 380 fs. The absorbed energy corresponds approximately to 9200 cm^{-1} in x and 9800 cm^{-1} in y direction, the uncertainty to 3900 cm^{-1} in x and to 3600 cm^{-1} in y direction. The lowest contour line has the value 4×10^{-5} u^{-1} pm^{-2}, the distance between them is 7×10^{-5} u^{-1} pm^{-2}. Maximal values are variable according to the number of contour lines shown.

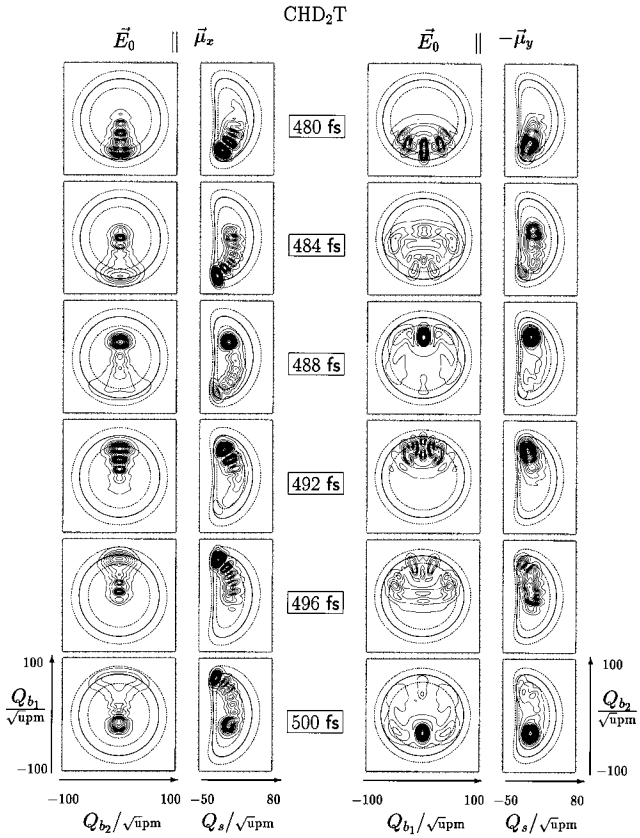

Figure 8. Snapshots of the time evolution of reduced two-dimensional probability as in Figure 7 (see also legend to that figure), but for a time interval between 480 and 500 fs. The absorbed energy corresponds to 13100 cm^{-1} in x and 13500 cm^{-1} in y direction, the uncertainty to 5300 cm^{-1} in x and to 4400 cm^{-1} in y direction. The lowest contour line has the value 4×10^{-5} u^{-1} pm^{-2}, the distance between them is 7×10^{-5} u^{-1} pm^{-2}. Maximal values are variable according to the number of contour lines shown.

from equilibrium. For CHD_2T, excitation along the x-axis is equivalent to forcing the wave packet to move along the Q_{b_1} manifold ($= Q_6$ in Table 1, CHD_2T). Along this manifold, significant displacements from equilibrium are possible, apart from the H-atom displacement along the x-axis, for the T- and the two D-atoms along the z-axis with nearly the same magnitude $\Delta z \approx 0.18\,|Q_{b_1}|$ but in opposite directions. Excitation along the y-axis corresponds to changing Q_{b_2} ($= Q_5$ in Table 1, CHD_2T), and leads to somewhat larger displacements of the deuterium atoms ($\Delta z \approx \pm 0.25 Q_{b_1}$), which could be the reason for a more efficient redistribution. If this idea is correct, axes should have inverted roles upon excitation of $CHDT_2$. Indeed, inspection of Table 1, $CHDT_2$ shows that displacements of the D-atom along Q_{b_2} ($= Q_6$ in Table 1, $CHDT_2$), corresponding to y-axis excitation, are small ($\Delta y \approx 0.04 Q_{b_2}$), while they are large for excitation along the x-axis ($\Delta z \approx 0.32 Q_{b_1}$, $Q_{b_1} = Q_5$ in Table 1, $CHDT_2$). Accordingly, the wave packet motion should be localized in the $\{Q_s, Q_{b_2}\}$-manifold in $CHDT_2$, after excitation along the y-axis, while it spreads efficiently into all three dimensions after excitation along the x-axis. Our calculations confirm this result.

In the following we discuss this aspect further in a more detailed analysis of the out-of-symmetry-plane bending excitation (y-excitation) in CHD_2T and $CHDT_2$ and the generation of dynamical chirality. For this purpose, we use a rectangular pulse with 30 TW cm^{-2} intensity at the wave numbers 1270 cm^{-1}, for CHD_2T, and 1200 cm^{-1}, for $CHDT_2$. Under these conditions we obtain efficient excitation and assure converged calculations in the first 300 fs of the excitation process. Figure 9 shows snapshots of the wave packet motion in CHD_2T during the excitation phase. We observe clearly that the superposition of an alternating squeezing and spreading of the wave packet on top of its semiclassical oscillations sets in smoothly, it is weaker at early stages (between 150 and 170 fs) and becomes stronger later (between 180 and 200 fs). The energy values in Figure 9 are $\langle E(t)/hc \rangle \approx 10600$ cm^{-1} ($\Delta E(t)/hc \approx 2600$ cm^{-1}), for all snapshots on the left- hand side, and $\langle E(t)/hc \rangle \approx 13100$ cm^{-1} ($\Delta E(t)/hc \approx 3300$ cm^{-1}), for all snapshots on the right-hand side (averaged values in the corresponding 20 fs time intervals, zero-point energy included).

At 200 fs the laser is switched off, and the wave packet is highly localized on one side of the symmetry plane, which can be defined here by the condition $Q_{b_2} = 0$. In Figure 10 we show the time evolution of the wave packet thereafter. Immediately after the laser has been switched off (200−224 fs), the wave packet first continues the semiclassical oscillatory motion, whereby the superposed, alternating spreading and squeezing becomes more pronounced, which is seen best in the bending−bending representation. The contour lines in the representations of the wave packets are equidistant. The lowest value shown is at 4×10^{-5} u^{-1} pm^{-2}, the distance between the lines is 7×10^{-5} u^{-1} pm^{-2}, and the maximal value is variable. It is lowest for a widely spread out wave packet, e.g., in the snapshot at 220 fs. Each wave packet yields unit probability if integrated over all coordinates. More values are listed in the figure captions.

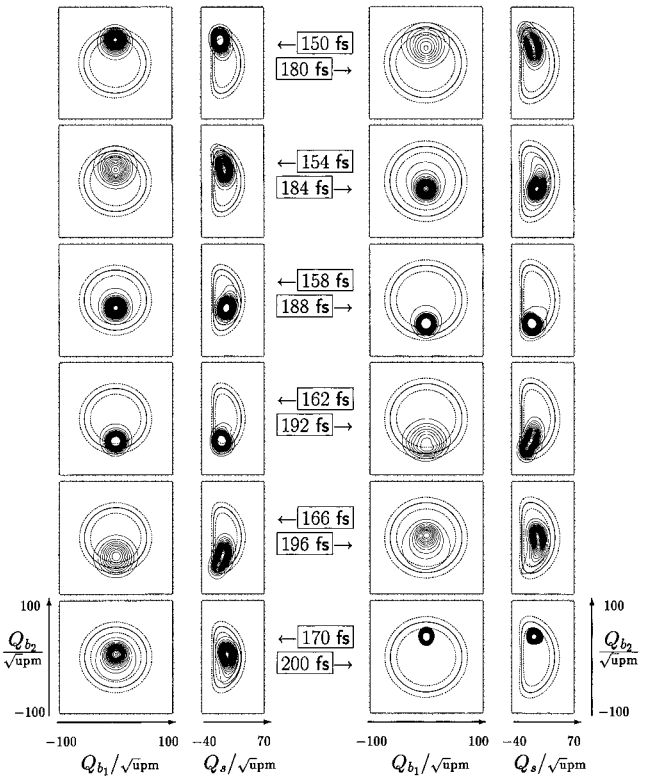

Figure 9. Snapshots of the time evolution of reduced two-dimensional probability densities during the excitation of CHD_2T along the *y*-axis with a laser tuned at 1270 cm^{-1} at an intensity of 30 TW cm^{-2} between 150 and 170 fs (left-hand side) and 180 to 200 fs (right-hand side; see also legend to Figure 5; here, all two-dimensional contour line representations have as vertical axis the Q_{b_2}-coordinate, and horizontal axes Q_{b_1} and Q_s). The absorbed energy corresponds to 7600 cm^{-1} between 150 and 170 fs and 10100 cm^{-1} between 180 and 200 fs, the uncertainties 2600 cm^{-1} and 3300 cm^{-1}, respectively. The lowest contour line has the value 4×10^{-5} u^{-1} pm^{-2}, the distance between them is 7×10^{-5} u^{-1} pm^{-2}. Maximal values are variable according to the number of contour lines shown.

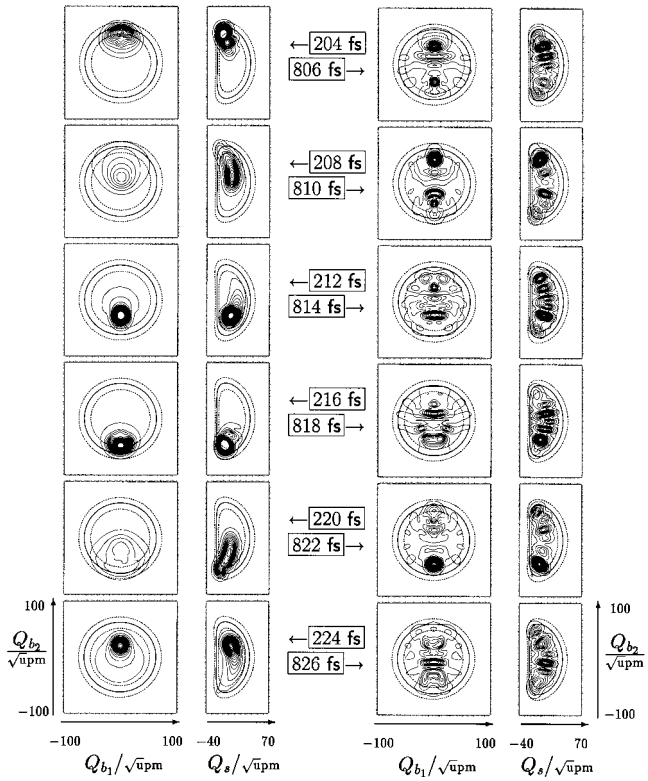

Figure 10. Snapshots of the free time evolution of reduced two-dimensional probability densities **after** the excitation of CHD_2T shown previously in Figure 9 (see also legend to that figure). The laser has been switched off at 200 fs. Absorbed energy and energy uncertainty are constant for all snapshots and have the same value as for the snapshot at 200 fs in Figure 9. The lowest contour line has the value 4×10^{-5} u^{-1} pm^{-2}, the distance between them is 7×10^{-5} u^{-1} pm^{-2}. Maximal values are variable according to the number of contour lines shown.

For much longer times, e.g., between 806 and 826 fs (right-hand side of Figure 10), the motion has become irregular, the original oscillations can hardly be recognized and the probability density is highly redistributed among all degrees of freedom of the CH chromophore system, both in the bending−bending and stretching−bending representations. The populations of spectroscopic states were determined by the excitation process at the time step 200 fs and are shown in Figure 13. These values remain constant throughout all snapshots after the excitation laser has been switched off.

As discussed above, in $CHDT_2$ the wave packet motion is localized after excitation along the *y*-axis. This is shown in Figure 11. The squeezing and spreading is clearly less pronounced here than for CHD_2T. At 212 fs the laser is switched off. The wave packet motion thereafter is shown in Figure 12. Redistribution of probability density occurs only into the stretching manifold, after long times. The probability density is then approximately homogeneously distributed in the $\{Q_{b_2}, Q_s\}$ subspace, the Q_{b_1} manifold remains nearly unoccupied. The energy values in Figure 12 are $\langle E(t)/hc \rangle \approx 13200$ cm^{-1} and $\Delta E(t)/hc \approx 3200$ cm^{-1}, very similar to the case of CHD_2T. The distribution of populations, which is constant after the laser has been switched off, is shown in Figure 14.

The comparison of Figures 13 and 14 shows that, in $CHDT_2$, only the lowest state within each polyad is populated, whereas for CHD_2T at least two to three states more in the center of each polyad can be efficiently populated by excitation along the *y*-axis. In the polyad with chromophore quantum number *N*, the lowest states are essentially those states with approximate bending quantum numbers $v_{b_1} \approx 2N$, $v_{b_2} \approx 0$ or $v_{b_1} \approx 0$, $v_{b_2} \approx 2N$, and $v_s \approx 0$ for stretching vibrations. These quantum numbers are only approximate, since the stretching and bending manifolds are anharmonically coupled. Central states can be mixed with $v_{b_1} \approx N$, and $v_{b_2} \approx N$. The confinement of the wave packet motion in the $\{Q_s, Q_{b_2}\}$ subspace, in case of $CHDT_2$, and the full three-dimensional redistribution of probability density for CHD_2T is related to the population distribution within each polyad. The stronger delocalization in CHD_2T can thus also be understood as arising from a broader distribution of population among semi-isoenergetic states which are strongly mixed.

One could expect that a more selective excitation in CHD_2T might be possible also upon excitation of the *y*-axis, if the excitation laser is tuned to lower wave numbers falling into the lower end of each polyad. However, excitation efficiency decreases very rapidly, as seen from the inserts in Figure 4a,b, which is directly related to excitation selection rules. Excitation along the *y*-axis requires an A'' state in the first step of the sequential multiphoton process. From Table 2 we see that the A'' state of CHD_2T is at the upper end of the first excited polyad ($N = 1/2$), while it is at the lower end for $CHDT_2$. This is an additional explanation for the inverted roles of selectivity upon *x*-axis excitation, which requires an A' state in the polyad $N = 1/2$. Excitation selectivity is thus also strongly linked with excitation efficiency.

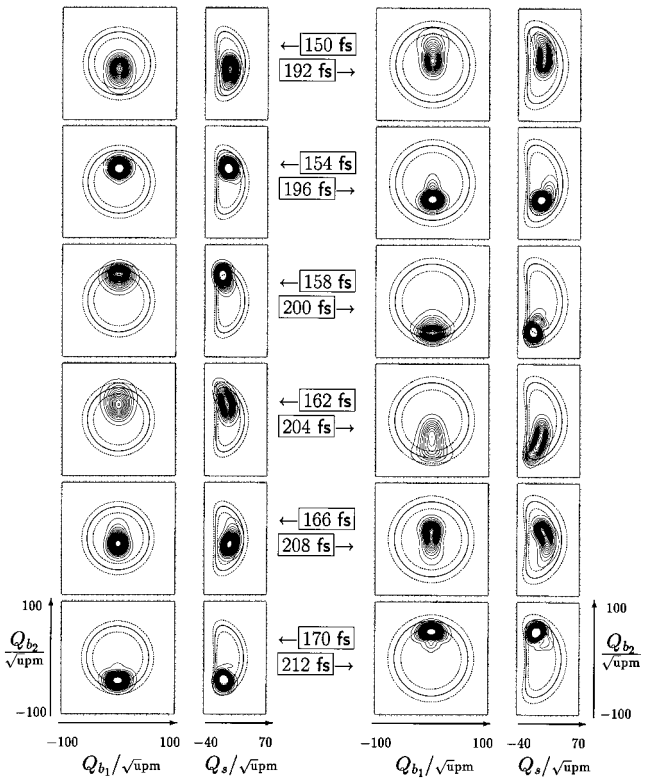

Figure 11. Snapshots of the time evolution of reduced two-dimensional probability densities during the excitation of $CHDT_2$ along the *y*-axis with a laser tuned at 1200 cm^{-1} at an intensity of 30 TW cm^{-2} between 150 and 170 fs (left-hand side) and 192 to 212 fs (right-hand side; see also legend to Figure 9). The absorbed energy corresponds to 7700 cm^{-1} between 150 and 170 fs and 11000 cm^{-1} between 192 and 212 fs, the uncertainties 2700 and 3700 cm^{-1}, respectively. The lowest contour line has the value 4×10^{-5} u^{-1} pm^{-2}, the distance between them is 7×10^{-5} u^{-1} pm^{-2}. Maximal values are variable according to the number of contour lines shown.

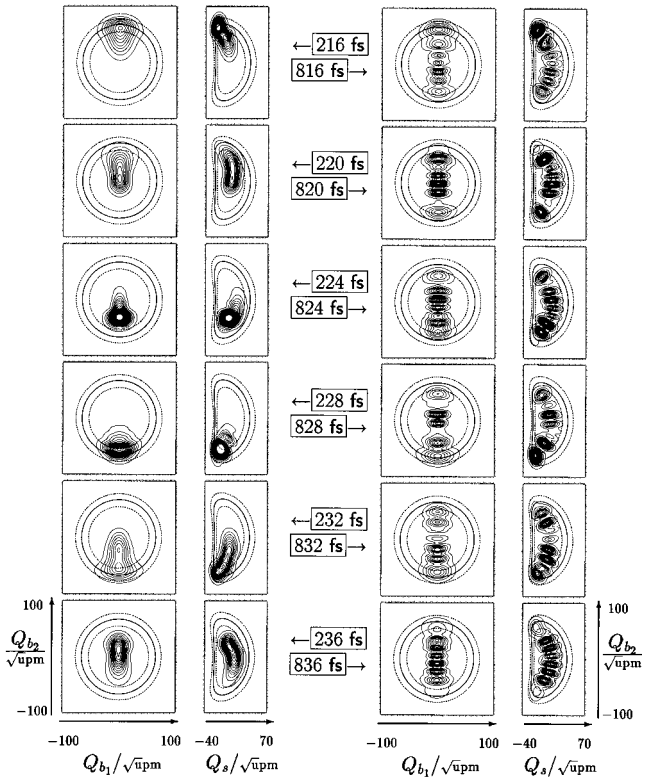

Figure 12. Snapshots of the free time evolution of reduced two-dimensional probability densities **after** the excitation of $CHDT_2$ shown previously in Figure 11 (see also the legend to that figure). The laser has been switched off at 212 fs. Absorbed energy and energy uncertainty are constant for all snapshots and have the same value as for the snapshot at 212 fs in Figure 11. The lowest contour line has the value 4×10^{-5} u^{-1} pm^{-2}, the distance between them is 7×10^{-5} u^{-1} pm^{-2}. Maximal values are variable according to the number of contour lines shown.

Before closing the section of wave packet motion we discuss, for completeness, the stretching excitation of the CH chromophore in CHD_3 under similar conditions as in Figures 5 and 6. As shown in the snapshot sequences of Figure 15, stretching excitation at 10 TW cm^{-2} is nearly as efficient as the excitation along the bending manifold during the initial excitation phase (between 50 and 60 fs, left-hand side in the figure). However, for later times (right-hand side in the figure), it is significantly less efficient than the bending excitation at comparable intensities. Energy values in Figure 15 are $\langle E(t)/hc \rangle \approx 6080$ cm^{-1} and $\Delta E(t)/hc \approx 1090$ cm^{-1}, for all snapshots on the left-hand side, and $\langle E(t)/hc \rangle \approx 6660$ cm^{-1} with $\Delta E(t)/hc \approx 2120$ cm^{-1}, on the right-hand side. The snapshots are separated by time intervals of 2 fs to account for the twofold faster stretching oscillations ($\tilde{\nu}_s \approx 3000$ cm^{-1}), and show that bending motion is less involved in this process up to this time interval.

At the intensity $I_0 = 30$ TW cm^{-2}, excitation along the *z*-manifold is significantly more efficient, as discussed in our previous work.[32] Here we have tested those results with calculations performed within the full CH chromophore space. The results are shown in Figure 16 and allow us to confirm the former results within the CH chromophore model.

3.4. Time-Dependent Enantiomeric Excess. The wave packet shown in the snapshot at 200 fs in Figure 9 is highly localized. It describes a chiral molecular structure with a well-defined chirality quantum number, say *R*, and enantiomeric excess $D_{abs} = 1$ from eq 1. As time evolves, the wave packet

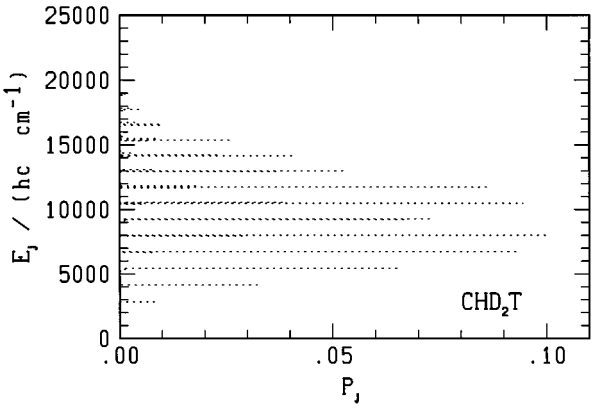

Figure 13. Population profile $P_J(t_0)$ at $t_0 = 200$ fs after excitation of CHD_2T along the *y*-axis as described in Figure 10.

moves to the other side of the symmetry plane $Q_{b_2} = 0$ implying a change of chirality. In the context of the present work, the enantiomeric excess can be defined by the probabilities

$$P_L(t) = \int_0^\infty \mathrm{d}Q_{b_2} \, |\psi_{b_2}(t, Q_{b_2})|^2 \tag{34}$$

$$P_R(t) = \int_{-\infty}^0 \mathrm{d}Q_{b_2} \, |\psi_{b_2}(t, Q_{b_2})|^2 \tag{35}$$

$$= 1 - P_L(\mathrm{t}) \tag{36}$$

for left-handed ("*L*") and right-handed ("R") chiral structures,

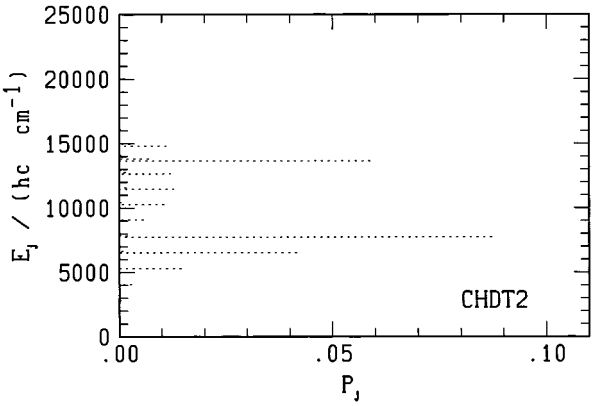

Figure 14. Population profile $P_j(t_0)$ at $t_0 = 212$ fs after excitation of $CHDT_2$ along the *y*-axis as described in Figure 12.

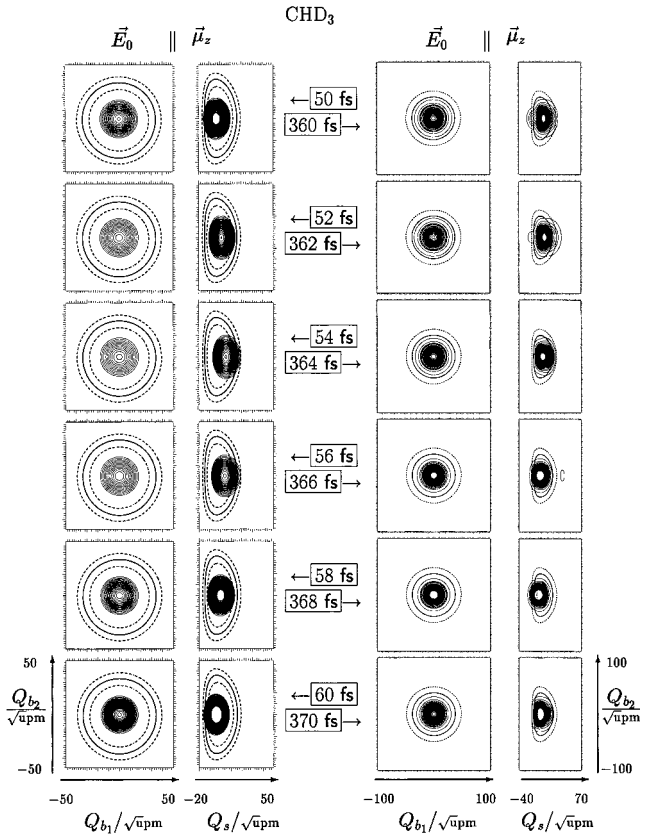

Figure 15. Snapshots of the time evolution of reduced two-dimensional probability densities during the excitation of CHD_3 along the *z*-axis with a laser tuned at 2815 cm^{-1} at an intensity of 10 TW cm^{-2} between 50 and 60 fs (left-hand side) and 360 to 370 fs (right-hand side; see also the legend to Figure 9). The absorbed energy corresponds approximately to 3200 cm^{-1} between 50 and 60 fs and 3819 cm^{-1} between 360 and 370 fs, the uncertainties 1100 and 2100 cm^{-1}, respectively. The lowest contour line has the value 44×10^{-5} u^{-1} pm^{-2}, the distance between them is 7×10^{-5} u^{-1} pm^{-2}. Maximal values are variable according to the number of contour lines shown.

where

$$|\psi_{b_2}(t, Q_{b_2})|^2 = \int_{Q_s}\int_{Q_{b_1}} \mathrm{d}Q_s \mathrm{d}Q_{b_1} |\psi(t, Q_s, Q_{b_1}, Q_{b_2})|^2 \quad (37)$$

The time evolution of $P_R(t)$ is shown in Figure 17 for the subsequent field-free motion of the wave packets described above in Figures 10, for CHD_2T, and 12, for $CHDT_2$. It should be stressed, that the dynamical chirality of a localized wave packet of CHD_2T or $CHDT_2$ corresponding to a bent structure

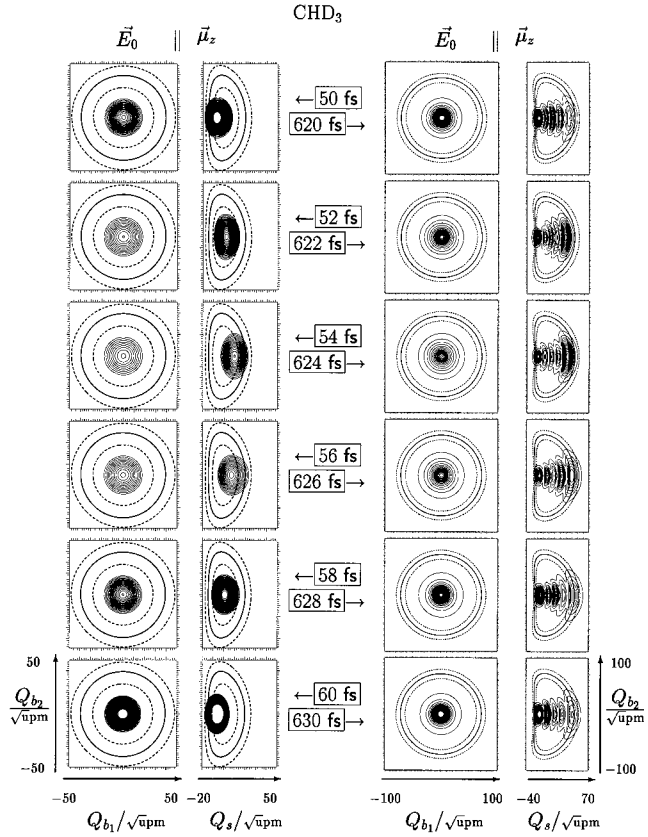

Figure 16. Snapshots of the time evolution of reduced two-dimensional probability densities during the excitation of CHD_3 along the *z*-axis with a laser tuned at 2815 cm^{-1} at an intensity of 30 TW cm^{-2} between 50 and 60 fs (left-hand side) and 620 to 630 fs (right-hand side; see also legend to Figure 9). The absorbed energy corresponds approximately to 4050 cm^{-1} between 50 and 60 fs and 13400 cm^{-1} between 620 and 630 fs, the uncertainties 2000 and 2700 cm^{-1}, respectively. The lowest contour line has the value 44×10^{-5} u^{-1} pm^{-2}, the distance between them is 7×10^{-5} u^{-1} pm^{-2}. Maximal values are variable according to the number of contour lines shown.

of C_1 symmetry has a well-defined, time-dependent, intrinsic sense of chirality, independent of external orientation in space (it would be conventionally classified as either *R* or *S*.[87]).

In the main part of each figure, the evolution of P_R calculated within the stretching and bending manifold of states for the CH chromophore is shown (solid continuous line). For the purpose of the following discussion, we also show the evolution of P_R within a one-dimensional model, where only the Q_{b_2} bending manifold is considered (interrupted line). The left-hand side insert shows a survey of the evolution of P_R for the one-dimensional case during a longer time interval of 2 ps, while the right-hand side insert shows the evolution of P_R for the calculation within the full three-dimensional stretching and bending manifold of states during the same time interval of 2 ps.

From the three-dimensional calculations, we observe a fast, initially nearly periodic evolution, with an approximate period of 30 fs, which is superimposed by a slower decay of probability corresponding to an overall decay of enantiomeric excess $|D_{abs}(t)| = |1 - 2P_R(t)|$ on a time interval of 300−400 fs for both CHD_2T and $CHDT_2$. The decay is clearly more pronounced for CHD_2T (Figure 17a). The first type of evolution corresponds to a stereomutation reaction, while the second can be interpreted as racemization. Comparison with the wave packet motion allows us to conclude that racemization is induced in this case by the presence of DIVR between the vibrational degrees of

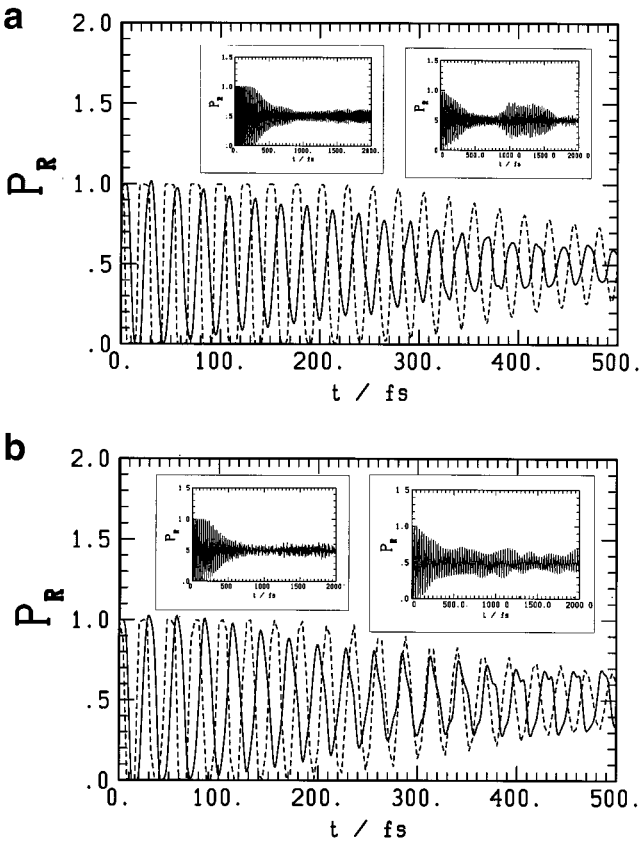

Figure 17. Evolution of the probablility for right-handed chiral structure $P_R(t)$ (see eq 35) of the CH chromophore in CHD_2T (a) and $CHDT_2$ (b) after preparation of chiral structures with multiphoton laser excitation, as discussed in Figures 9 and 11 (solid continuous line). For comparison, the time evolution of P_R according to one-dimensional model calculations including only the Q_{b_2} bending mode (interrupted line) are also shown. The left-hand insert shows the time evolution of P_R within the one-dimensional calculations for a longer time interval, while the right-hand insert shows the P_R time evolution within the three-dimensional calculation for the same time interval (see text).

freedom. Racemization is stronger for CHD_2T, for which DIVR occurs in the full three-dimensional subspace of the CH chromophore, under the present conditions. It is less pronounced for $CHDT_2$, which has a higher degree of localization of the wave packet motion.

According to the 1D calculations, an initial periodic evolution with a period of 30 fs and a decay of the overall enantiomeric excess is observed for CHD_2T, as well as for $CHDT_2$. The decay takes place on a time scale of 500−600 fs. As before, we interpret the periodic evolution as a stereomutation reaction while the decay corresponds to a racemization. The enantiomeric decay is now slightly slower than in the three-dimensional case. Since in the one-dimensional calculations the bending mode considered is as anharmonic as in the three-dimensional calculations, it can be further concluded that the one-dimensional bending anharmonicity qualitatively describes racemization on longer time scales whereas it is of secondary importance for the enantiomeric decay in the first 200 fs.

3.5. Effective Basis States. In this section we discuss the nature of the effective basis states χ_k^{eff} calculated by eq 20. We shall show that, indeed, such states can be identified with the "Fermi modes" introduced in our previous work, if appropriate phase conventions are assumed. For brevity, the discussion will be restricted to the subset of the 7 effective basis states $\{\chi(\upsilon_s,\upsilon_b)|\upsilon_s + (1/2)\upsilon_b = 6, l_b = 0\}$ in CHD_3 which are defined

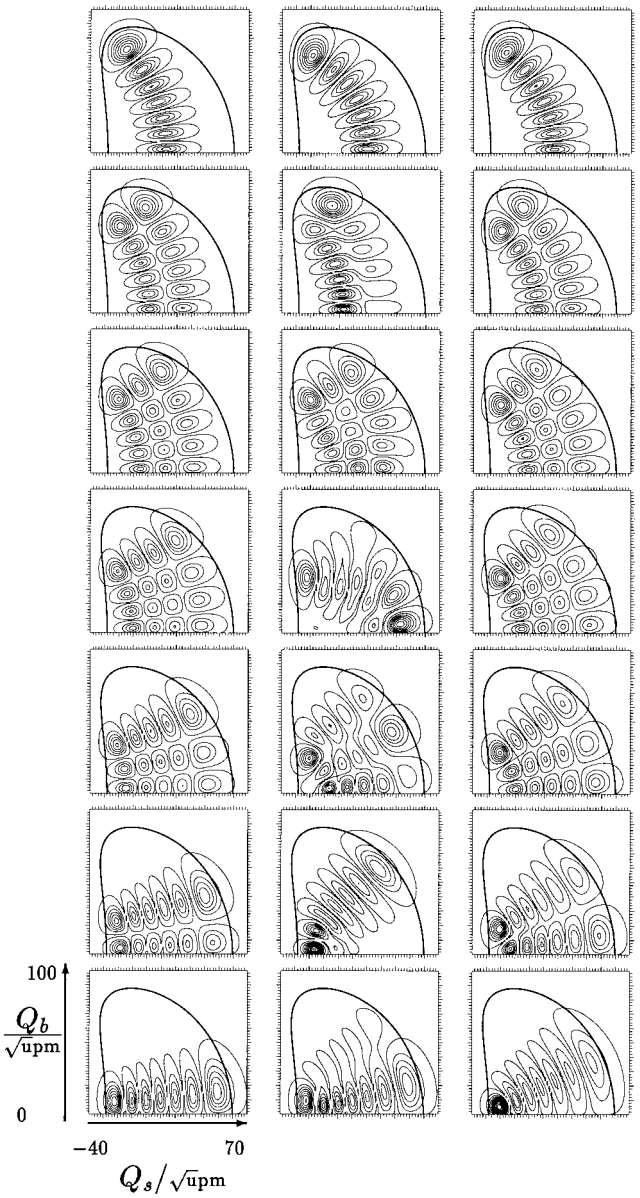

Figure 18. Probability densities $|\psi(Q_s,Q_b|^2$ in cylindrical coordinates corresponding to eq 38 for vibrational states of CHD_3 belonging to the energy level defined by the chromophore quantum number $N = 6$ and the vibrational angular momentum quantum number $l_b = 0$. Right-most column: Eigenstates N_7 to N_1 (N_j nomenclature in $C_{\infty v}$ symmetry, see Table 2 and ref 46). Mid column: Effective basis states defined by eq 20 and convention 1 (see text). Left-most column: Effective basis states defined by eq 20 and convention 2 (see text).

by the chromophore quantum number $N = 6$ and the quantum number $l_b = 0$.

Figure 18 shows probability densities

$$|\psi(Q_s, Q_b)|^2 = \int_0^{2\pi} Q_b d\phi_b |\psi(Q_s, Q_b, \phi_b)|^2 \qquad (38)$$

in a cylindrical representation of wave functions, where $Q_b = \sqrt{Q_{b_1}^2 + Q_{b_2}^2}$ and $\phi_b = \arctan(Q_{b_1}/Q_{b_2})$. The column at the right-hand side shows the densities of the eigenstates $\{\phi_{N_j}|N = 6, l_b \approx 0\}$. The solid lines are sections of the potential energy surface at the average energy of these states (corresponding roughly to 16000 cm^{-1}). The eigenstates have a well-defined nodal structure along curvilinear coordinates, which may be called ρ_s and φ_b.[46] To identify these coordinates, we look at the eigenfunction with lowest energy within this polyad, shown in

the uppermost row: It has 6 nodes along φ_b and 0 nodes along ρ_s. The eigenfunction with highest energy is shown at the bottom row and has 6 nodes along ρ_s and 0 nodes along φ_b. These coordinates are of the hyperspherical type[88,89] and the total nodal pattern is such that $n_s + n_b = 6$, where n_s is the number of nodes along ρ_s and n_b is the number of nodes along φ_b.

The center column shows representations of effective basis states. Here, we have chosen the convention that the sign of the largest element in all column vectors $\mathbf{Z}$ and $\mathbf{Z}^{eff}$ must be positive, which we call our *convention 1* (see Section 2 for the definition of column vectors). The nodal pattern is clearly less well defined here, apart perhaps for a few states. Although these states correspond to physically accessible states, since they are superpositions of eigenstates, they do not provide a direct and physically meaningful interpretation of the effective Fermi resonance Hamiltonian.

In contrast to that, the column on the left-hand side shows a well-defined nodal structure. This shows effective basis states, which were calculated within our *convention 2*: $\mathrm{sign}(Z_{k^*,N_j}) = \mathrm{sign}(Z^{eff}_{k^*,N_j})$, where k^* represents the effective basis state with $v_s = N$ and $v_b = 0$. Within this convention, we found that the same result is obtained, if one takes for k^* the basis state with $v_s = 0$ and $v_b = 2N$. The nodal structure can be used to define a new set of curvilinear coordinates R_s and R_b, which are evidently quite different from the curvilinear coordinates ρ_s and φ_b. An approximate analytical representation of these coordinates has been modeled by us previously,[32] and can be cast into the form

$$R_s \approx Q_s + AQ_b^2 \exp(2BQ_s) \tag{39}$$

$$R_b \approx Q_b \exp(BQ_s) \tag{40}$$

where A and B are transformation parameters related to the Fermi resonance coupling constant K'_{sbb}. In ref 32, these coordinates were called "Fermi modes".

Indeed, once an appropriate convention for the relative phases between the column vectors of $\boldsymbol{Z}$ and $\boldsymbol{Z}^{eff}$ has been established, the procedure proposed by eq 20 allows one to calculate effective basis states and make a one-to-one correspondence to the eigenstates with respect to the nodal structure. The diagonalization of the underlying effective Hamilton matrix can then also be performed, to a certain approximation, by an appropriate rotation of the effective basis states in the $\{Q_s,Q_b\}$ space, since they are nearly degenerate.[90,91]

4. Conclusions and Outlook

The analysis of high-resolution infrared spectra in conjunction with ab initio calculations provides accurate "experimental" Hamiltonians and potential energy and electric dipole hypersurfaces for polyatomic molecules even of the complexity of methane.[55,56] Using these results, we have investigated the time-dependent quantum dynamics of the CH chromophore in the methane isotopomers CHD_3, CH_2DT, and $CHDT_2$ by calculation of the wave packet motion during and after coherent multiphoton excitation of vibrational motion at wave numbers in the region of the bending fundamentals. At present, within the CH chromophore model, we neglect the influence of large amplitude molecular vibrations other than the CH stretching and bending modes. The amplitude of those vibrations are small, under the conditions of our calculations, and they are likely to become important at later times than considered here.[32] We also disregard the slower reorientation in space due to the overall molecular rotational motion in the laboratory frame.

The following main conclusions can be drawn from our investigations:

1. Coherent excitation of bending modes is more efficient than stretching excitation.[32] Larger displacements of the wave packet from equilibrium can be achieved with less intensity.

2. Intramolecular vibrational redistribution of the classical type (CIVR)[25] exists and is represented by a semiclassical motion of the wave packet in the multidimensional configuration space. It is similar to a Lissajous type of motion[53] along a path in the stretching−bending representation in accordance with the principle of least action. CIVR is more long lived and more pronounced for the bending excitation than for stretching. However, as observed before for the stretching excitation,[32] the delocalized type of intramolecular vibrational redistribution (DIVR)[25] sets in at later stages of the dynamics, roughly after 300−500 fs of excitation.

3. Isotopic substitution leads to separation of excitation pathways. Excitation of bending modes along the *x*- and *y*-axis in a molecule-fixed frame are then differently efficient. While excitation along the *y*-axis leads to full three-dimensional DIVR in CHD_2T, vibrational redistribution in $CHDT_2$ is only two-dimensional, within the time scale of our calculation. Excitation along the *x*-axis inverts the roles for the two isotopomers.

4. A relative phase difference of the wave packet motion between the bending directions of CHD_3, induced by locking the phase between the *x*- and *y*-excitation, remains unaltered, even after the spreading of the wave packet and the collapse of the semi-classical dynamics. For CH_2DT and $CHDT_2$ this phase shift changes during the evolution of the wave packet.

5. Dynamical chirality can be generated upon multiphoton excitation of a large amplitude, semi-classical wave packet motion of the out-of-plane bending vibration of the CH chromophore in the asymmetric tops CH_2DT and $CHDT_2$. The free evolution of such a prepared wave packet leads initially to a nearly periodic exchange of right- and left-handed chiral structure, corresponding to a stereomutation reaction on the time scale of 30 fs. On top of this motion, for times of 300−400 fs and with the start of DIVR, racemization starts substituting the evolution and leads to small values of the enantiomeric excess D_{abs}. This effect is entirely due to the coherent quantum dynamics in our calculations and is more pronounced for CH_2DT, where DIVR occurs in a larger subspace than for $CHDT_2$, at least in the time scales and conditions considered here. These results on stereomutation and racemization within the framework of quantum chemical kinetics can be considered to provide the extreme limit of low barrier enantiomerization (i.e., zero barrier). It can be compared to low barrier tunneling stereomutation in multidimensional kinetics[40−43] as well as to our earlier 1d model of controlling stereomutation.[39]

6. The set of wave functions corresponding to the basis states which give rise to the effective Hamiltonian have been finally identified after an appropriate choice of phases between transformation matrices. They have a regular nodal pattern along curvilinear coordinates which we have called "Fermi modes".

Clearly, CIVR is at the heart of a redistribution process which sets in after 100−200 fs already, leading to a wave packet motion along both stretching and bending manifolds, although still highly localized in shape. One question is then, whether the stretching parts of this wave packet can be eliminated, for example within an intelligent manipulation of the wave packet evolution in such a way as to force the wave packet to move in a direction orthogonal to the stretching manifold to reach even larger amplitudes of bending motion. One strategy for such a control mechanism would be the generation of "bending" and

"stretching" pulse sequences to cool down the stretching motion. The idea is that "bending" pulses, i.e., at wave numbers in the region of the bending fundamentals of the CH chromophore will mainly excite the bending modes, with some leaking out into the stretching manifolds due to IVR. "Stretching" pulses, i.e., at wave numbers in the region of the stretching fundamentals could then potentially be used as a damping procedure for the stretching contamination.

It is possible that the differences observed for the intramolecular vibrational redistribution after bending excitation of CHD_2T and $CHDT_2$ become less pronounced, if the excitation process takes much more time, i.e., at an apparently more unfavorable excitation wave number which would lead to stronger mixing of states also in case of $CHDT_2$. Also, we have not yet considered the possibility of exciting CHD_3 with a circularly polarized pulse (in the molecule-fixed *xy*-plane), rather than with linearly polarized pulses as treated here. This has the potential of producing localized wave packet motion of large amplitude in the bending manifold of symmetric molecules.[92] Another interesting extension of the present investigation of methane isotopomers (or derivative) quantum dynamics concerns stereomutation in the high barrier limit (say, for the CHDTMu isotopomer[55,83]) with very long time wave packet evolution including potential effects from the parity violating weak nuclear interaction.[93−95]

Acknowledgment. Help from and discussions with David Luckhaus and Jürgen Stohner are gratefully acknowledged. Our work is supported financially by Schweizerischer Nationalfonds and ETH Zürich (including also CSCS and AGS project).

References and Notes

(1) Faraday Discussion No. 75 on Intramolecular Dynamics. *J. Chem. Soc. Faraday Discuss.* **1983**, *75*, (in particular also the introductory article by C. S. Parmenter).
(2) *Faraday Discuss. Chem. Soc.* **1986**, *82*. On the dynamics of photofragmentation.
(3) Femtochemistry. *J. Phys. Chem.* **1993**, *97*, Issue 48.
(4) *Femtosecond Chemistry*; Manz, J., Wöste, L., Eds.; *Proc. Berlin Conf. Femtosecond Chemistry, Berlin, March 1993;* Verlag Chemie: Weinheim, 1995.
(5) *Femtosecond Reaction Dynamics;* Wiersma, D. A., Ed.; North-Holland: Amsterdam, 1994.
(6) Quack, M.; Kutzelnigg, W. *Ber. Bunsenges. Phys. Chem.* **1995**, *99*, 231−245.
(7) XXth Solvay Conference on Chemistry: Chemical Reactions and Their Control on the Femtosecond Time Scale *Adv. Chem. Phys.* **1997**, *101*.
(8) *Ultrafast Phenomena X*, Vol. 62 of *Springer Series in Chemical Physics;* Barbara, P. F., Fujimoto, J. G., Knox, W. H., Zinth, W., Eds.; Springer: Heidelberg, 1996.
(9) *J. Phys. Chem.* **1998**, *102*, Issue 23.
(10) Zewail, A. H. *J. Phys. Chem.* **1993**, *97*, 12427−12446.
(11) Owrutsky, J. C.; Raftery, D.; Hochstrasser, R. M. *Annu. Rev. Phys. Chem.* **1994**, *45*, 519−555.
(12) Fleming, G. R.; Joo, T.; Cho, M. *Adv. Chem. Phys.* **1997**, *101*, 141−180.
(13) Dobler, J.; Zinth, W.; Kaiser, W.; Oesterhelt, D. *Chem. Phys. Lett.* **1988**, *144*, 215−220.
(14) Schoenlein, R. W.; Peteanu, L. A.; Mathies, R. A.; Shank, C. V. *Science* **1991**, *254*, 412−415.
(15) Baumert, T.; Helbing, J.; Gerber, G. *Adv. Chem. Phys.* **1997**, *101*, 47−82.
(16) Uji, L.; Jager, F.; Atkinson, G. H. *Biophys. J.* **1998**, *74*, 1492−1501. Atkinson, G. H. at Int. Conf. TRVS IX, Tucson, 1999.
(17) El-Sayed, M. A. Paper at Int. Conf. TRVS IX, Tucson, 1999.
(18) Anfirud, P. A.; Lim, M.; Jackson, T. A. Paper at Int. Conf. TRVS IX, Tucson, 1999.
(19) Laenen, R.; Laubereu, A. Paper at Int. Conf. TRVS IX, Tucson, 1999.
(20) Tasumi, M.; Nakabayashi, T.; Okamoto, H. Paper at Int. Conf. TRVS IX, Tucson, 1999.
(21) Kobayashi, T.; Shirakawa, A. Paper at Int. Conf. TRVS IX, Tucson, 1999.
(22) Porter, G. In *Femtosecond Chemistry*; Manz, J., Woeste, L., Eds.; *Proc. Berlin Conf. Femtosecond Chemistry, Berlin, March 1993*, pages 3−13 and 625−632, Weinheim, 1995. Verlag Chemie. Chapters 1 and 21.
(23) Quack, M. In *Femtosecond Chemistry*; Manz, J., Woeste, L., Eds.; *Proc. Berlin Conf. Femtosecond Chemistry, Berlin, March 1993*, pages 781−818, Weinheim, 1995. Verlag Chemie. Chapter 27.
(24) Quack, M. *Annu. Rev. Phys. Chem.* **1990**, *41*, 839−874.
(25) Quack, M. *J. Mol. Struct.* **1993**, *292*, 171−195.
(26) Lehmann, K. K.; Scoles, G.; Pate, B. H. *Annu. Rev. Phys. Chem.* **1994**, *45*, 241−274.
(27) Nesbitt, D. J.; Field, R. W. *J. Phys. Chem.* **1996**, *100*, 12735−12756.
(28) Field, R. W.; O'Brien, J. P.; Jacobson, M. P.; Solina, S. A. B.; Polik, W. F.; Ishikawa, H. *Adv. Chem. Phys.* **1997**, *101*, 463−490.
(29) Neusser, H. J.; Neuhauser, R. *Adv. Chem. Phys.* **1997**, *101*, 409−447.
(30) Beil, A.; Luckhaus, D.; Quack, M.; Stohner, J. *Ber. Bunsenges. Phys. Chem.* **1997**, *101*, 311−328.
(31) Marquardt, R.; Quack, M.; Stohner, J.; Sutcliffe, E. *J. Chem. Soc., Faraday Trans. 2* **1986**, *82*, 1173−1187.
(32) Marquardt, R.; Quack, M. *J. Chem. Phys.* **1991**, *95*, 4854−4867.
(33) Quack, M.; Stohner, J. *J. Phys. Chem.* **1993**, *97*, 12574−12590.
(34) Luckhaus, D.; Quack, M.; Stohner, J. *Chem. Phys. Lett.* **1993**, *212*, 434−443.
(35) Quack, M. *Angew. Chem., Int. Ed. Engl.* **1989**, *28*, 571−586.
(36) Lupo, D. W.; Quack, M. *Chem. Rev.* **1987**, *87*, 181−216.
(37) Crim, F. F. *J. Phys. Chem.* **1996**, *100*, 12725−12734.
(38) Kohler, B.; Krause, J. L.; Raski, F.; Wilson, K. R.; Yakovlev, V. V.; Whitnell, R. M.; Yan, Y. *Acc. Chem. Res.* **1995**, *28*, 133−140.
(39) Marquardt, R.; Quack, M. *Z. Physik D* **1996**, *36*, 229−237.
(40) Kuhn, B.; Rizzo, T. R.; Luckhaus, D.; Quack, M.; Suhm, M. *J. Chem. Phys.* **1999**, *111*, 2565−2587.
(41) Fehrensen, B.; Luckhaus, D.; Quack, M. *Chem. Phys. Lett.* **1999**, *300*, 312−320.
(42) Fehrensen, B.; Hippler, M.; Quack, M. *Chem. Phys. Lett.* **1998**, *298*, 320−328.
(43) Fehrensen, B.; Luckhaus, D.; Quack, M. *Z. Phys. Chem. N. F.* **1999**, *209*, 1−19.
(44) Rice, S. A. *Adv. Chem. Phys.* **1997**, *101*, 213−283.
(45) Jacobson, M. P.; O'Brien, J. P.; Silbey, R. J.; Field, R. W. *J. Chem. Phys.* **1998**, *109*, 121−133.
(46) Lewerenz, M.; Quack, M. *J. Chem. Phys.* **1988**, *88*, 5408−5432.
(47) Quack, M. *J. Chem. Soc., Faraday Discuss.* **1994**, *99*, 388−395.
(48) Child, M. S.; Lawton, R. T. *Faraday Discuss. Chem. Soc.* **1981**, *71*, 273−285.
(49) He, Y.; Pochert, J.; Quack, M.; Ranz, R.; Seyfang, G. *J. Chem. Soc., Faraday Discuss.* **1995**, *102*, 358−362, 372−375.
(50) Quack, M. In *Encyclopedia of Computational Chemistry, Vol. 3;* Ragué Schleyer, P. v., Allinger, N., Clark, T., Gasteiger, J., Kollman, P. A., Schaefer, H. F., III, Schreiner, P. R., Eds.; John Wiley and Sons, New York, 1998; pages 1775−1791.
(51) Marquardt, R.; Quack, M. *Infrared Phys.* **1989**, *29*, 485−501.
(52) Marquardt, R.; Quack, M. *J. Chem. Phys.* **1989**, *90*, 6320−6327.
(53) Herzberg, G. *Molecular Spectra and Molecular Structure III. Electronic Spectra and Electronic Structure of Polyatomic Molecules;* Van Nostrand Reinhold Co., New York, reprint (1991) ed., 1966.
(54) Quack, M. *J. Mol. Struct.* **1995**, *347*, 245−266.
(55) Marquardt, R.; Quack, M. *J. Chem. Phys.* **1998**, *109*, 10628−10643.
(56) Hollenstein, H.; Marquardt, R.; Quack, M.; Suhm, M. A. *J. Chem. Phys.* **1994**, *101*, 3588−3602.
(57) Quack, M.; Sutcliffe, E. *QCPE Bull.* **1986**, *6*, 98.
(58) Marquardt, R.; Quack, M.; Stohner, J. To be published.
(59) Luckhaus, D.; Quack, M. *Chem. Phys. Lett.* **1992**, *190*, 581−589.
(60) Beil, A.; Luckhaus, D.; Marquardt, R.; Quack, M. *J. Chem. Soc., Faraday Discuss.* **1994**, *99*, 49−76.
(61) Gray, D. L.; Robiette, A. G. *Mol. Phys.* **1979**, *37*, 1901−1920.
(62) Iung, C.; Leforestier, C. *J. Chem. Phys.* **1992**, *97*, 2481−2489.
(63) Iung, C.; Leforestier, C. *J. Chem. Phys.* **1994**, *102*, 8453−8461.
(64) Baggott, J. E.; Chuang, M.-C.; Zare, R. N.; Dübal, H. R.; Quack, M. *J. Chem. Phys.* **1985**, *82*, 1186−1194.
(65) Boyarkin, O. V.; Settle, R. D. F.; Rizzo, T. R. *Ber. Bunsenges. Phys. Chem.* **1995**, *99*, 504−513.
(66) Maynard, A. T.; Wyatt, R. E.; Iung, C. *J. Chem. Phys.* **1995**, *103*, 8372−8390.
(67) Hippler, M.; Quack, M. *J. Chem. Phys.* **1996**, *104*, 7426−7430.
(68) Maynard, A. T.; Wyatt, R. E.; Iung, C. *J. Chem. Phys.* **1997**, *106*, 9483−9496.
(69) Signorell, R.; Marquardt, R.; Quack, M.; Suhm, M. A. *Mol. Phys.* **1996**, *89*, 297−313.
(70) Loesch, H. J.; Remscheid, A. *J. Chem. Phys.* **1990**, *93*, 4779−4790.
(71) Friedrich, B.; Herschbach, D. *Phys. Rev. Lett.* **1995**, *74*, 4623−4626.

(72) Kim, W.; Felker, P. M. *J. Chem. Phys.* **1996**, *104*, 1147−1150.
(73) Seideman, T. *J. Chem. Phys.* **1995**, *103*, 7887−7896.
(74) Felker, P. M.; Zewail, A. H. In *Femtosecond Chemistry*; Manz, J., Woeste, L., Eds.; *Proc. Berlin Conf. Femtosecond Chemistry, Berlin, March 1993*, pp 193−260, Weinheim, 1995. Verlag Chemie. Chapter 5.
(75) Hervé, S.; Le Quéré, F.; Marquardt, R. Rotational and vibrational wave packet motion of HF during IR multiphoton excitation. To be published.
(76) Quack, M.; Sutcliffe, E. *Chem. Phys. Lett.* **1983**, *99*, 167−172.
(77) Quack, M.; Sutcliffe, E. *Chem. Phys. Lett.* **1984**, *105*, 147−152.
(78) Quack, M.; Sutcliffe, E. *J. Chem. Phys.* **1985**, *83*, 3805−3812.
(79) Quack, M. *J. Chem. Phys.* **1978**, *69*, 1282−1307.
(80) Donley, E.; Marquardt, R.; Quack, M.; Stohner, J.; Thanopulos, I.; Wallenborn, E. U. To be submitted.
(81) Quack, M. *Adv. Chem. Phys.* **1982**, *50*, 395−473.
(82) Wilson, E. B., Jr.; Decius, J. C.; Cross, P. C. *Molecular Vibrations. The Theory of Infrared and Raman Vibrational Spectra;* McGraw-Hill Book Company, Inc., 1955.
(83) Marquardt, R.; Quack, M. To be published.
(84) Luckhaus, D.; Quack, M. *Chem. Phys. Lett.* **1993**, *205*, 277−284.
(85) Davis, K. A.; Ewing, G. E. *J. Chem. Phys.* **1998**, *107*, 8073−8082.
(86) Friedrich, B.; Herschbach, D. *Z. Phys. D* **1996**, *36*, 221−228.
(87) Cahn, R. S.; Ingold, C.; Prelog, V. *Angew. Chem., Int. Ed. Engl.* **1966**, *5*, 385; IUPAC Nomenclature of Organic Chemistry Section E (Stereochemistry), Rigaudy, J., Klesney, S., Eds.; Pergamon: Oxford, 1979.
(88) Bisseling, R. H.; Kosloff, R.; Manz, J. *J. Chem. Phys.* **1985**, *83*, 993−1004.
(89) Bisseling, R. H.; Kosloff, R.; Manz, J.; Mrugała, F.; Römelt, J.; Weichselbaumer, G. *J. Chem. Phys.* **1987**, *86*, 2626−2638.
(90) Louck, J. D.; Moshinski, M.; Wolf, K. B. *J. Math. Phys.* **1973**, *14*, 692.
(91) Martens, C. C.; Ezra, M. S. *J. Chem. Phys.* **1987**, *87*, 284.
(92) Pochert, J.; Quack, M.; Seyfang, G. In preparation.
(93) Bakasov, A.; Ha, T. K.; Quack, M. *J. Chem. Phys.* **1998**, *109*, 7263−7285.
(94) Berger, R.; Quack, M. *J. Chem. Phys.* **2000**, *112*, 3148−3158.
(95) Quack, M.; Stohner, J. *Abstracts Book SASP 2000; Phys. Rev. Lett.* **2000**, *84*, 3807.
(96) Dupre-Maquaire, J. *J. Mol. Spectrosc.* **1983**, *101*, 319−324.
(97) Permogorov, D.; Campargue, A.; Chenevier, M.; Ben Kraiem, H. *J. Mol. Spectrosc.* **1995**, *170*, 10−26.
(98) Campargue, A.; Stoeckel, F.; Chenevier, M.; Ben Kraiem, H. *J. Chem. Phys.* **1987**, *87*, 5598−5605.
(99) Ben Kraiem, H.; Campargue, A.; Chenevier, M.; Stoeckel, F. *J. Chem. Phys.* **1989**, *91*, 2148−2152.
(100) Domingo, C.; del Olmo, A.; Escribano, R.; Bermejo, D.; Orza, J. M. *J. Chem. Phys.* **1992**, *96*, 972−975.